Highlights

Variability of the Weddell Sea Deep Waters in GLORYS12v1 Reanalysis

Marina Noro, Tiago S. Dotto, Marcos Tonelli, Ilana Wainer

- WDW shows a spurious freshening trend.
- WSDW and WSBW trends are overestimated relative to observations.
- Decadal deep water variability is tied to the Weddell Gyre strength and sea ice cover.

Variability of the Weddell Sea Deep Waters in GLORYS12v1 Reanalysis

Marina Noro[a,*], Tiago S. Dotto[b], Marcos Tonelli[c], Ilana Wainer[a]

[a] *Department of Physical Oceanography, Oceanographic Institute of the University of São Paulo, Praça do Oceanográfico, 191, Butantã, São Paulo, São Paulo, Brazil*
[b] *National Oceanography Centre, European Way, Southampton, SO14 3ZH, UK*
[c] *Admiral Paulo Moreira Institute for Sea Studies, Brazil Navy, Rua Kioto, 253, Arraial do Cabo, 28930-000, Rio de Janeiro, Brazil*

Abstract

Understanding deep-water variability in the Weddell Sea remains a challenge, given the limited observational coverage and the difficulties ocean models face in representing fine-scale processes, particularly along the Antarctic margin. Recent high-resolution oceanic products offer a valuable opportunity to advance understanding of this region. Nevertheless, it is crucial to critically evaluate their reliability before relying on them for scientific analysis. Here, we assess the representation and variability of Warm Deep Water (WDW), Weddell Sea Deep Water (WSDW), and Weddell Sea Bottom Water (WSBW) in the 1/12° Global Ocean Physics Reanalysis (GLORYS12v1) between 1993 and 2020. GLORYS12v1 reproduces key hydrographic features and vertical stratification below 500 m, despite persistent biases in the upper ocean. WDW shows a spurious freshening trend and a cool bias in Section SR4, diverging from the observed neutral salinity and warming trend. Moreover, WSDW and WSBW exhibit overestimated warming and salinification trends. These discrepancies are primarily linked to (i) a weakening of the Weddell Gyre, which limits inflow and renewal of deep waters; (ii) stronger westerlies enhancing Ekman transport and upwelling; and (iii) changes in sea ice concentration affecting deep convection. A complex maximum covariance analysis reveals strong decadal-scale covariability between the Weddell Gyre barotropic circulation and the thermohaline structure of

*Corresponding author
Email address: marina.noro.santos@usp.br (Marina Noro)

deep water masses, especially WSDW and WSBW. Although GLORYS12v1 resolves many relevant processes, its overestimation of trends and underrepresentation of coastal dynamics highlight the need for improved vertical coordinate schemes, refined mixing parameterizations, and enhanced observational coverage to better capture the variability of deep waters in polar regions.

Keywords: High-Resolution Ocean Reanalysis, Antarctic Bottom Water, Subpolar Gyre, Sea Ice

1. Introduction

The Antarctic Bottom Water (AABW) ventilates a substantial fraction of the global abyssal ocean, since it feeds the lower limb of the Global Overturning Circulation (Lumpkin and Speer, 2007; Talley, 2013). From the 1980s to the 2000s, AABW experienced warming, accounting for approximately 10% of the total uptake of ocean heat in the global abyssal ocean (depths $>$ 4000 m) and the deep Southern Ocean (1000–4000 m) (Purkey and Johnson, 2010; Azaneu et al., 2013). It also experienced volume loss at a rate of -8.2 ($\pm$2.6) $\times$ 10^6 m^3 s^{-1} in the Southern Ocean (Fahrbach et al., 2011; Purkey and Johnson, 2012; Azaneu et al., 2013; Zhou et al., 2023). Specifically in the Weddell-Enderby basin, the AABW contraction of -3.6 $\pm$ 2.0 Sv is equivalent to an average isotherm descent of $\approx$ 15 m yr^{-1} (Purkey and Johnson, 2012). Recent findings not only support this long-term trend but also reveal a 30% reduction in the volume of AABW exported from the Weddell Sea between 1992 and 2020 (Zhou et al., 2023), and a weakening of its northward transport into the North Atlantic of about 12 $\pm$ 5% since 2000 (Biló et al., 2024). These changes are thought to be related to a reduction in the formation rates of this water mass (Zhou et al., 2023). Therefore, evaluating the variability and changes of the precursors of AABW is essential to understand the fate of the lower limb of the Global Overturning Circulation (Li et al., 2023).

In this study, we focus on the Weddell Sea (Figure 1a), a major AABW export region. The circulation in the Weddell Sea is characterized by the coupling of the Weddell Gyre and the abyssal overturning pathway, which involves the formation and export of AABW, driven by winds and buoyancy fluxes (Naveira Garabato et al., 2016; Vernet et al., 2019). The cyclonic Weddell Gyre is the primary large-scale feature of the Weddell Sea circulation, and has a mean volume transport of 45–56 Sv (Klatt et al., 2005). Westerly

winds in the northern gyre and easterly winds in the southern gyre induce divergent Ekman transport, which drives upwelling of Warm Deep Water (WDW) at the center of the gyre and its downwelling along coastal margins (Klatt et al., 2005; Naveira Garabato et al., 2016; Vernet et al., 2019).

At the western and southern shelf breaks of the Weddell Sea, Dense Shelf Water (DSW; formed during sea ice formation or interaction with ice shelves) interacts with the intermediate WDW (found between 200 and 1500 m, with temperature $\theta > 0°C$) or its modified form–a mixture of WDW with the shallower near-freezing minimum temperature surface Winter Water at 50 and 200 m (Carmack and Foster, 1975; Orsi et al., 1993; Kerr et al., 2009)–as it descends as a plume along the continental slope. The mixing between these water masses gives rise to the deep water masses (depths greater than 1500 m) in the Weddell Gyre, which comprise two distinct local variations of the AABW: Weddell Sea Deep Water (WSDW; $0°C < \theta < -0.7°C$) and Weddell Sea Bottom Water (WSBW; $\theta < -0.7°C$) (Figure 1b; Carmack and Foster, 1975; Schröder and Fahrbach, 1999; Meredith et al., 2000; Fahrbach et al., 2004). WSBW is restricted to the Weddell Sea Abyssal Plain by a system of submarine ridges (Orsi et al., 1993; Fahrbach et al., 1994). In contrast, WSDW is exported by the western boundary current of the Weddell Gyre (Naveira Garabato et al., 2002; Le Paih et al., 2020) and constitutes the primary component of AABW (Orsi et al., 1993; Fahrbach et al., 1994; Kerr et al., 2009).

Despite its crucial role, monitoring the abyssal layer of AABW, especially near its source regions, has been challenging. Understanding ocean dynamics on various scales is crucial for identifying the ocean's response to ongoing climate change and predicting how it will evolve in future climate change scenarios. Observations provide invaluable direct measurements, but they are often sparse in both time and space, particularly in the deep ocean and polar regions, where they are also summer-biased. Climate models, on the other hand, offer a process-based understanding of ocean circulation and provide future projections, but struggle to resolve key physical interactions. In this context, ocean reanalysis products emerge as a valuable tool to improve our understanding of ocean dynamics by combining the strengths of observations and models to create a spatially and temporally continuous dataset. However, their reliability depends on the quality and coverage of assimilated observations as well as the accuracy of the underlying model physics, particularly in poorly observed deep layers. Therefore, given these limitations, ocean reanalyses should be validated to assess whether they accurately cap-

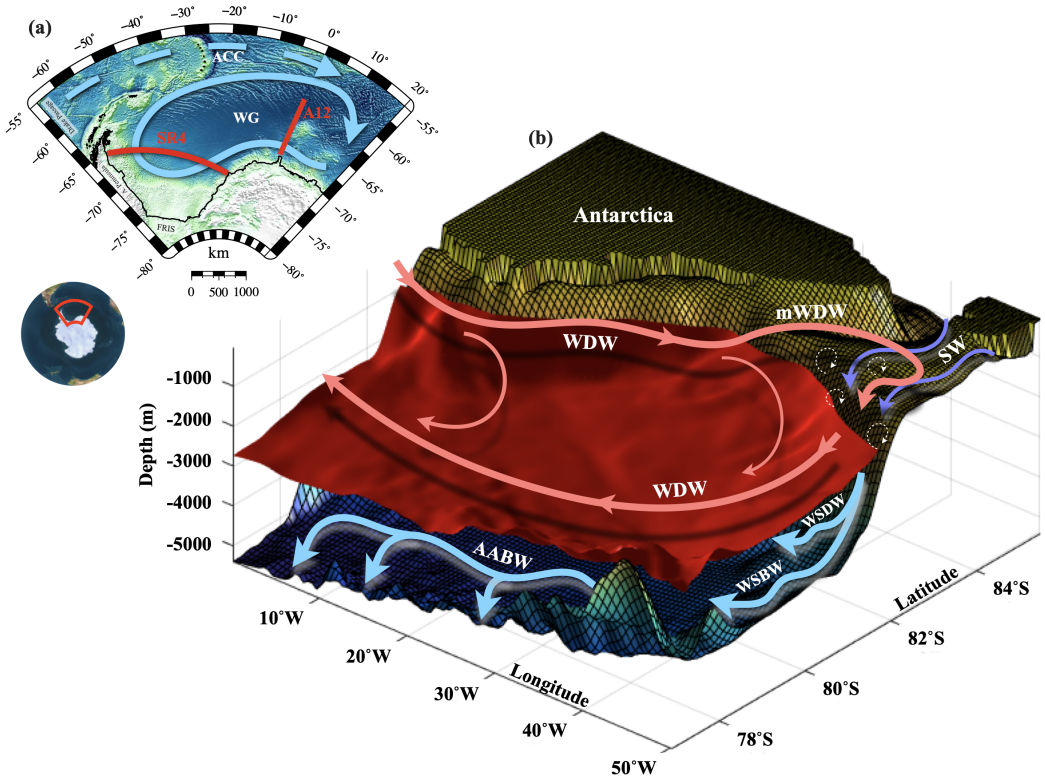

Figure 1: **Schematic of the Weddell Gyre circulation, reproduced from Tonelli et al. (2019)** (a) Bathymetry of the Atlantic sector of the Southern Ocean centered on the Weddell Sea. The solid blue arrow represents the Weddell Gyre (WG) circulation, while the dashed blue arrow represents the Antarctic Circumpolar Current (ACC). The red solid lines mark Sections SR4 and A12. (b) Perspective of the Weddell Sea multi-layer circulation, depicting the near–shelf break interactions between the WDW (coral arrow) and the supercooled Shelf Waters (SW; purple arrows), whose mixing forms WSDW and WSBW, which are ultimately exported as AABW (light blue arrows).

ture hydrographic variability and trends before being used as ground truth, especially in deep layers (Dotto et al., 2014; Azaneu et al., 2014; Aguiar et al., 2017; Nakayama et al., 2024).

Here, we assess the representativeness and variability of WDW, WSDW, and WSBW in the Weddell Sea in the eddy-resolving Global Ocean Physics Reanalysis 1/12° (GLORYS12v1). We compared the properties, stratification, and variability of the simulated water mass with available observational products and previous studies in the Weddell Sea (e.g., Fahrbach et al., 2011; Kerr et al., 2018).

2. Methods

2.1. Global Ocean Physics Reanalysis 1/12° (GLORYS12v1)

GLORYS12v1, provided by the Copernicus Marine Environment Service (CMEMS), is a global eddy-resolving physical ocean and sea ice reanalysis with a horizontal resolution of 1/12° and 50 vertical levels, covering the altimetry era from 1993 onward. GLORYS12v1 aims to provide a reliable representation of the physical ocean state, serving as a key tool to support climate and marine environment policies (Lellouche et al., 2021; Drévillon et al., 2022a).

The system configuration used in GLORYS12v1 is based on the current real-time global CMEMS high-resolution forecasting system, which uses the Nucleus for European Modeling of the Ocean (NEMO; Madec and The NEMO Team, 2008) version 3.1 coupled with version 2 of the Louvain-la-Neuve sea ice Model (LIM2; Fichefet and Maqueda, 1997; Goosse and Fichefet, 1999; Lellouche et al., 2018, 2021; Drévillon et al., 2022a), and the associated effects of changes in sea ice volume are reflected in sea level variability under the Boussinesq approximation (Drévillon et al., 2022b). The physical configuration is based on the tripolar Oceanic Reliable foreCAst at 1/12° (ORCA12) grid (Madec and Imbard, 1996), with a horizontal resolution of 9.25 km at the equator, 7 km at mid-latitudes, 4.5 km at subpolar latitudes, and 2 km towards the Ross and Weddell seas. The vertical grid is based on z-level coordinates, discretized from 1 m in the upper layers to 450 m in the deepest layers (Lellouche et al., 2018, 2021). The bathymetry is based on the Earth TOPOgraphy 1 arc-minute Global Relief Model (ETOPO1)6 (Amante and Eakins, 2009), for regions deeper than 300 m, and General Bathymetric Chart of the Oceans (GEBCO8) (Becker et al., 2009), with a

30-arc second resolution global topography/bathymetry grid, in regions shallower than 200 m with a linear interpolation in the layer of 200-300 m and does not include ice shelf cavities (Lellouche et al., 2018; Drévillon et al., 2022a).

GLORYS12v1 is initialized with temperature and salinity fields from EN-ACT/ENSEMBLES version 4.2.0 (EN4) monthly gridded climatology (Good et al., 2013). The surface forcing comes from the European Centre for Medium-Range Weather Forecasts Re-Analysis Interim (ERA-Interim) between 1993 and 2018 and by ERA version 5 (ERA5) reanalysis from January 1st, 2019 (Hersbach et al., 2020; Drévillon et al., 2022a). The surface turbulent fluxes of heat and momentum are derived from the Large and Yeager (2009) bulk formulae, which consider the presence of sea ice. Observations assimilated include: reprocessed along-track altimeter sea level anomaly from CMEMS (Pujol et al., 2016), National Oceanic and Atmospheric Administration 1/4° daily Optimum Interpolation sea surface temperature (Huang et al., 2021), sea ice concentration from the Ifremer Centre ERS d'Archivage et de Traitement (CERSAT) database, and *in situ* temperature and salinity profiles from CMEMS COriolis Re-Analysis version 4.1 (CORAv4.1) (Szekely et al., 2023), which include Argo data and profiles from sea mammals (Lellouche et al., 2021; Drévillon et al., 2022a).

GLORYS12v1 reanalysis applies the Boussinesq approximation and does not directly represent the global mean steric effect on sea level. To maintain consistency with assimilated satellite observations of sea level anomalies, a globally diagnosed mean steric sea level trend is added at each time step to the modeled dynamic sea level (see Lellouche et al., 2025 for more details). Additionally, to prevent drift in the mean sea surface height caused by uncertainties in the global water budget, (1) the global freshwater budget is constrained to follow a prescribed seasonal cycle based on observational estimates (Chen et al., 2005), retaining only spatial deviations from this mean; and (2) a long-term trend is introduced to the surface mass budget to account for freshwater input from glacier and ice sheet mass loss in Greenland and Antarctica (Lellouche et al., 2018, 2021).

To quantify uncertainty, Drévillon et al. (2022b) provided an estimated global model–observation statistics for temperature and salinity across depth layers for the period 1993–2016. These values represent typical global uncertainties used to evaluate the reliability of GLORYS12v1 against observational assimilated data, and provide a reference for assessing the magnitude of regional differences observed in the Weddell Sea (presented in Section 3.1). No

uncertainty estimates are available for depths below 2000 m, as long-term and regionally representative observations of the deep ocean are not yet available. In these deeper layers, GLORYS12v1 relies on virtual vertical profiles of temperature and salinity constructed from the monthly climatology of the World Ocean Atlas (WOA) 2013 (Lellouche et al., 2018, 2021).

In this study, we computed the annual averages of potential temperature (θ), practical salinity (S), eastward and northward current velocities, and sea ice concentration (SIC) from the monthly outputs. Our analyses focused primarily on the corresponding locations of the long-term hydrographic repeat sections A12, along the Greenwich Meridian, and, in this study, limited to latitudes south of 60°S, and SR4, crossing the Weddell Sea basin (Figure 1a). We evaluated annual averages because (i) we found a weak seasonal signal in water mass properties in GLORYS12v1, and (ii) the dominant variability occurs at interannual timescales (not shown). This temporal resolution aligns with the timescales of the dominant variability in the deep ocean, thereby reducing the impact of the sparse and irregular temporal sampling biases from the observations. Furthermore, our analysis focuses on ocean layers deeper than 500 m, thereby minimizing the influence of upper-layer biases (although this is briefly shown in Section 3.1).

2.2. Observational data products and methods for reanalysis evaluation

The large-scale picture is provided by the statistically objectively analyzed climatological fields of θ (Locarnini et al., 2019) and S (Zweng et al., 2019) from the WOA released in 2018 (WOA18; Garcia et al., 2019). WOA18 has a horizontal resolution of $1/4°$ and 102 vertical levels, ranging from a vertical spacing of 5 m in the upper 100 m and gradually decreasing to 100 m intervals between 2000 m and 5500 m depth (Locarnini et al., 2013). WOA18 uses quality-controlled oceanographic profile data from the World Ocean Database 2018 (Boyer et al., 2018). It incorporates data from bottle samples, high-resolution Conductivity-Temperature-Depth, profiling floats, moored and drifting buoys, gliders, undulating oceanographic recorders, Mechanical Bathythermographs, Digital Bathythermographs, Expendable Bathythermographs, and pinniped-mounted Conductivity-Temperature-Depth sensors. For salinity, it also includes data from ship-mounted thermosalinographs to integrate the surface data set.

WOA18 spans the 1955–2017 period and provides six decadal means of in situ temperature and S (Locarnini et al., 2019; Zweng et al., 2019). In this study, we restrict the periods of 1995–2004 and 2005–2017, based on

GLORYS12v1 outputs. We then averaged GLORYS12v1 outputs over these periods to produce mean fields comparable to WOA18 climatology. To enable direct comparison, we converted WOA18 in situ temperature to θ, interpolated the GLORYS12v1 fields to a horizontal resolution of $1/4°$, and interpolated the WOA18 climatological fields to match the 50 vertical levels used in GLORYS12v1. We compared GLORYS12v1 and WOA18 using simple differences of the hydrographic properties and θ-S diagrams.

Following Kerr et al. (2018), we defined the water mass layers based on their neutral density (γ^n; Jackett and McDougall, 1997) limits (Table 1 and Figure A.1). We then assessed the interannual variability of these layers in GLORYS12v1 against available hydrographic data from the repeated sections in the Weddell Sea collected during years overlapping with the reanalysis period (Table 2).

The root-mean-squared error (RMSE) between observations and reanalysis was calculated for each section to evaluate the accuracy of GLORYS12v1. We determined the standard deviation of the observed hydrographic parameters as the threshold to quantitatively characterize systematic biases and assess the reliability of GLORYS12v1 in representing the hydrographic structure and variability of the Weddell Sea water masses. We calculated trends in GLORYS12v1 using the non-parametric Mann-Kendall test at the 95% confidence level to assess the statistical significance of temporal changes.

Table 1: Limits of neutral density (γ^n) for Weddell Sea deep water masses.

Water Mass	γ^n **(kg·m^{-3})**
WDW	$28.10 \leq \gamma^n < 28.27$
WSDW	$28.27 \leq \gamma^n < 28.40$
WSBW	$\gamma^n \geq 28.40$

2.3. Barotropic Transport

We calculated the barotropic streamfunction (BSF) to evaluate how well the reanalysis captures the strength and structure of the Weddell Gyre and understand how variations in the gyre's strength influence the water masses, thereby impacting the regional heat and salt fluxes. The BSF represents the vertically integrated flow field, typically expressed in Sverdrups [1Sv = 10^6 m^3 s^{-1}], and is a widely used diagnostic to characterize large-scale circulation patterns. The BSF (ψ) was calculated offline, following Neme et al. (2021), as the meridional integral of the zonal mass transport integrated in depth (M_x):

Table 2: Hydrographic observations from repeated sections used in this study. Details about the instruments and their accuracy can be found in Driemel et al. (2017).

Expedition	Cruise Period (dd/mm/yyyy)	Section	Reference
ANT-X7	03/12/1992–22/01/1993	SR4	Fahrbach and Rohardt (1993)
ANT-XIII/4	17/03/1996–20/05/1996	A12 and SR4	Fahrbach and Rohardt (1996)
ANT-XV/4	28/03/1998–23/05/1998	A12 and SR4	Fahrbach and Rohardt (1998)
ANT-XVI/2	09/01/1999–16/03/1999	A12	Rohardt and Harms (2010)
ANT-XVIII/3	05/12/2000–12/01/2001	A12	Schröder (2010)
ANT-XX/2	24/11/2002–23/01/2003	A12	Schröder and Wisotzki (2010)
ANT-XXII/3	22/01/2005–06/04/2005	A12 and SR4	Rohardt (2010)
ANT-XXIV/3	10/02/2008–16/04/2008	A12 and SR4	Fahrbach and Rohardt (2008)
ANT-XXVII/2	28/11/2010–05/02/2011	A12 and SR4	Rohardt et al. (2011)
ANT-XXIX/2	02/12/2012–14/01/2013	A12	Rohardt (2013)
ANT-XXX/2	02/12/2014–31/01/2015	A12	Rohardt and Boebel (2015)

$$\psi(t,\lambda,\phi) = \int_{\phi_s}^{\phi} \left(\int_{H(\lambda,\phi)}^{0} \frac{M_x(t,\lambda,\phi,z)}{\rho_0}\, dz \right) d\phi \tag{1}$$

where λ represents longitude, ϕ represents latitude, $H(\lambda,\phi')$ is the depth of the ocean floor, and ρ_0 is the reference density of 1035 kg·m^{-3}. Integration was carried out from the southernmost latitude (ϕ_s) to the latitude of interest, and from the bottom to the ocean surface, ensuring that the streamfunction is zero at the boundaries. Setting $\psi = 0$ at the southern boundary provides a reference point for integration and ensures physical consistency, preventing artificial net transport across land boundaries. Finally, M_x is given by:

$$M_x(t,\lambda,\phi,z) = \rho(t,\lambda,\phi,z)\, u(t,\lambda,\phi,z)\, d\phi\, dz \tag{2}$$

where ρ represents the seawater density, and $d\phi$ and dz correspond to the sizes of the meridional and depth cells, respectively. For the top cell, we calculated the time-varying height by adding the sea surface height anomaly to the height of the top grid cell. We then multiplied this adjusted height by the velocity in the top cell to account for the time-varying transport at the surface.

2.4. Wind Stress

To evaluate the influence of atmospheric circulation on water mass variability, we calculated the momentum flux using the Large and Yeager (2009) bulk formulae, consistent with the formulation used in GLORYS12v1 (Lellouche et al., 2021):

$$\tau^x = \rho_a C_a |u_a| u_a \tag{3}$$
$$\tau^y = \rho_a C_a |v_a| v_a \tag{4}$$

where $\rho_a = 1.25$ kg m^{-3} is the air density, $C_a = 1.25 \times 10^{-3}$ is the air–water drag coefficient (Tsamados et al., 2014), and u_a and v_a are the zonal and meridional 10-m wind components, respectively. For wind velocities, we utilized the ERA5 reanalysis.

2.5. Complex Maximum Covariance Analysis

We applied complex Maximum Covariance Analysis (MCA) to identify dominant patterns of coupled variability between BSF, winds, and sea ice,

along with the hydrographic parameters of WDW, WSDW, and WSBW. The complex MCA is an extension of the traditional MCA method, described by Rieger et al. (2021). The analysis provides information on both the spatial patterns of covariability and the temporal evolution of these patterns through the associated amplitude and phase fields. The amplitude represents the strength of the covariance at each location, while the phase gives insight into the lagged or propagating nature of the relationship between the two fields. This method is well-suited for capturing the interannual and decadal variability observed in our study and for exploring potential mechanisms driving changes in the deep waters of the Weddell Sea.

The method converts each spatial field into complex variables by associating real and imaginary components of each input field using the Hilbert transform to construct the analytical signal ($\hat{\mathbf{X}}_\mathbf{s}$):

$$\hat{\mathbf{X}}_\mathbf{s} = \mathbf{X}_\mathbf{s} + i \cdot \mathscr{H}(\mathbf{X}_\mathbf{s}) \tag{5}$$

where $\mathbf{X}_\mathbf{s} \in \mathbb{R}$ is a spatiotemporal data field and $\mathscr{H}(\cdot)$ is the column-wise applied Hilbert transform. The components of the Hilbert transform are phased-shifted by $-\pi/2$ with respect to the original signal, which represents a signal that arrives with a lag of one-fourth of the typical period (Rieger et al., 2021).

The covariance between the two complex fields is then calculated, and the modes of covariability are obtained by solving the singular value decomposition of the complex covariance matrix. Each mode, ranked by the amount of covariance they explain, represents a coupled pattern between the two fields, with an associated singular value indicating the strength of covariability.

3. Results

3.1. Mean state of the water column structure and water mass properties

The upper layer of the Weddell Sea is composed of Antarctic Surface Water (AASW; $\theta < 0$°C) and a near-freezing remnant of the isothermal winter mixed layer known as Winter Water ($\theta < -1.7$°C; (Carmack, 1990; Whitworth et al., 1998; Fahrbach et al., 2004). Both GLORYS12v1 and WOA18 reproduce the AASW (Figure 2), but the reanalysis notably underrepresents the Winter Water. The larger θ and S differences between GLORYS12v1 and WOA18 are found in the upper layer. θ differences reach approximately 0.8°C in Section A12 (Figures 3c) and up to 1.5°C in Section SR4 (Figure

3f). These differences exceed the global bias of –0.05°C (-0.02°C) and RMSE of 0.97°C (0.85°C) for the 0–100 (100–300) m layer, calculated by Drévillon et al. (2022b). For the S of the upper layer, the differences are around 0.2 psu in both sections, comparable to the global RMSE values of 0.293 psu and 0.165 psu in the upper 300 m. While the global assessment indicates that the largest biases in GLORYS12v1 occur between 50 and 100 m depth, biases persist to greater depths in the Weddell Sea. In Section A12, θ and S differences remain above global estimates down to approximately 200 m, extending deeper north of 60°S near the Antarctic Circumpolar Current. In Section SR4, larger differences reach depths of 400 m or even greater near the continental slope at 10°W.

At intermediate layers, the WDW θ in GLORYS12v1 is lower than θ in WOA18 (Figures 3c and 3f), with differences up to -0.30°C. The WDW S, is slightly higher in GLORYS12v1 than in WOA18, with differences up to 0.01 psu in Section A12. In Section SR4, the 34.70 psu isohaline delineated the inflow and outflow WDW cores in the reanalysis. At WOA18, the same isohaline extends throughout the section without a clear representation of the WDW cores (Figures 3j,k). At depths associated with the 34.70 psu isohaline, GLORYS12v1 is up to 0.07 psu fresher than WOA18. Below 1000 m, GLORYS12v1 shows slightly higher S, with differences up to 0.01 psu (Figure 3l). These differences fall within the range of biases reported by Drévillon et al. (2022b) in the global quality assessment of GLORYS12v1. For the 300–800 m layer, the global mean temperature bias was -0.005°C with an RMSE of 0.48°C, while the salinity was -0.001 psu with an RMSE of 0.082 psu. In the 800–2000 m layer, the mean temperature bias was 0.006°C with an RMSE of 0.20°C, and the salinity mean bias was zero with an RMSE 0.054 psu (Drévillon et al., 2022b). Compared to these global values, the Weddell Sea θ and S differences are comparable to, and generally within, the expected range of reanalysis uncertainty documented for GLORYS12v1.

Below 2000 m, θ differences reach up to -0.4°C in the Weddell Sea. This result suggests the occurrence of colder deep waters in GLORYS12v1 in both sections (Figures 3c and 3f), which is also evident in the θ-S diagrams (Figure 2). The WSBW θ and S is generally < -0.7°C (Carmack and Foster, 1975; Fahrbach et al., 2004), a characteristic that is present in GLORYS12v1 but not in WOA18.

In general, GLORYS12v1 captures the vertical structure and stratification of the water column in the Weddell Sea relatively well. Despite biases in the upper ocean being more pronounced than the global average, GLORYS12v1

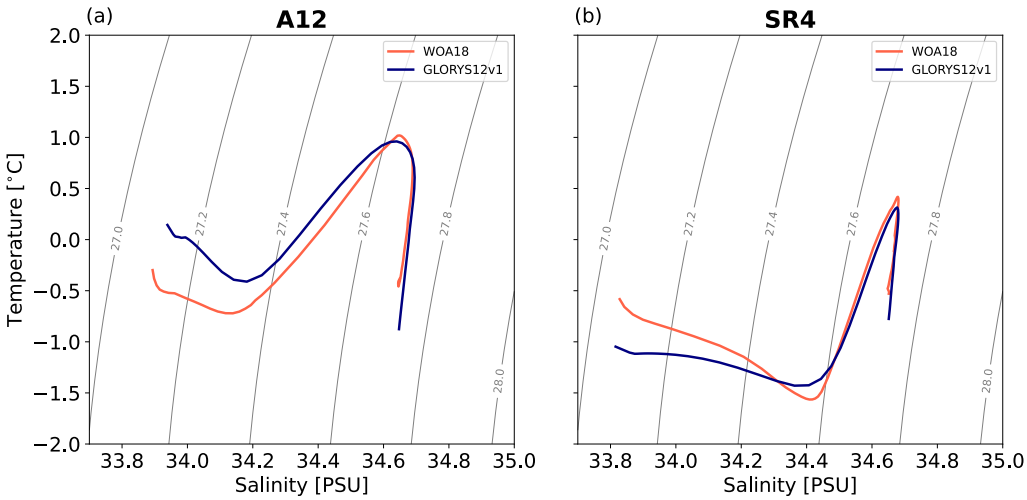

Figure 2: **Temperature and salinity structure from GLORYS12v1 and WOA18 (1995–2017).** θ-S diagrams for the A12 (a) and SR4 (b) sections based on GLORYS12v1 reanalysis (dark blue line) and WOA18 climatology (light orange line).

provides a reasonable representation of the intermediate layer. Additionally, GLORYS12v1 also captures key features of the Weddell Sea region. In Section A12 (Figure 3a,b), along the Greenwich Meridian, it is possible to observe the northern boundary of the Weddell Gyre around 56°S, where the core of the warmer Circumpolar Deep Water (CDW) from the Antarctic Circumpolar Current meets the colder WDW from the Weddell Sea, delineating the Weddell Front, as previously described by observations (Klatt et al., 2005; Fahrbach et al., 2004, 2011). Furthermore, due to the upwelling in the center of the gyre, there is a noticeable upward displacement of the isolines (Fahrbach et al., 2004), which is also evident in Section SR4 (Figure 3d,e).

In the next section, we analyze the temporal variability of the water masses considering only layers below 500 m to minimize the influence of large biases identified in the upper 400 m. Additionally, in Section A12, the analysis was further restricted to latitudes south of 60°S to include only the Weddell Sea hydrography.

3.2. Temporal variability of the Weddell Sea deep water masses

Comparison of annual averages of hydrographic parameters obtained from GLORYS12v1 along sections A12 and SR4 reveals that, unlike the mean fields (Figure 3), the water masses are warmer and saltier than the observation

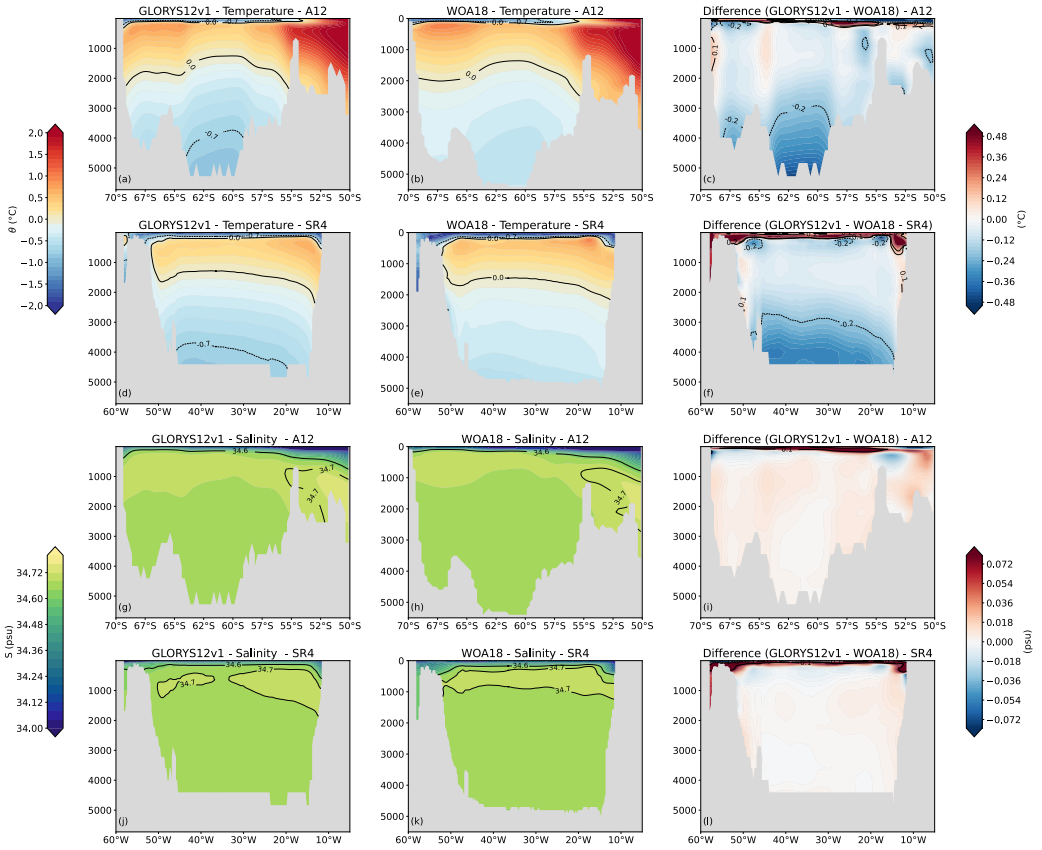

Figure 3: **Potential temperature (θ) and salinity (S) cross-sections (1995–2017 mean).** Panels (a–c, g–i) show θ and S, respectively, along section A12, while panels (d–f, j–l) show the same variables along section SR4. For each section, the first two panels (GLORYS12v1 and WOA18) are followed by the corresponding difference (GLORYS12v1 – WOA18).

snapshots (see Discussion for more details), resulting in denser water masses (Figures 4g–i and 5g–i). Despite the differences in the absolute values of the hydrographic properties, GLORYS12v1 captures the temporal variability of the water masses relatively well after 1996; i.e., GLORYS12v1 follows the highs and lows of the observed θ and S, particularly in Section A12.

From 1993 to 1995, GLORYS12v1 shows a pronounced decline in θ and S of the WDW in both sections, and in S of the WSDW in Section A12 (Figures 4a,d–b,e and 5a,d). Such declines are not evident in the observations at Section SR4, which include data before 1996. Therefore, caution must be taken when using the reanalysis for this period, as it may yield a spurious result. Thus, trends in these water masses were analyzed from 1996 to 2020.

For the WDW, trends were found only in S, which shows a freshening at a rate of $-2.7\pm1.0\times10^{-4}$ psu yr^{-1} in Section A12 and $-2.7\pm0.8\times10^{-4}$ psu yr^{-1} in Section SR4 (Figures 4d and 5d). In Section SR4, although fewer observations are available, they suggest that WDW properties remained relatively stable until 2008. From 2008 to 2011, the observations show an increase of approximately 0.1°C in θ and 0.005 psu in S of the WDW. This warming is not followed by GLORYS12v1, which, in contrast, shows relatively colder temperatures from 2008 onwards.

Table 3: RMSE of each hydrographic parameter for each water mass and section. The corresponding standard deviation (σ) of the observational data is also reported as a reference threshold to evaluate the reanalysis accuracy.

		Section A12	σ_{A12}	Section SR4	σ_{SR4}
WDW	θ (°C)	7.24×10^{-2}	1.97×10^{-1}	7.82×10^{-2}	2.30×10^{-1}
	S (psu)	7.90×10^{-3}	8.50×10^{-3}	9.30×10^{-3}	1.35×10^{-2}
	γ^n (kg m^{-3})	1.22×10^{-2}	3.14×10^{-2}	1.97×10^{-2}	3.34×10^{-2}
WSDW	θ (°C)	8.60×10^{-2}	1.79×10^{-1}	5.99×10^{-2}	1.82×10^{-1}
	S (psu)	5.30×10^{-3}	5.30×10^{-3}	4.30×10^{-3}	7.30×10^{-3}
	γ^n (kg m^{-3})	2.17×10^{-2}	3.46×10^{-2}	2.82×10^{-2}	3.63×10^{-2}
WSBW	θ (°C)	7.81×10^{-2}	4.00×10^{-2}	1.32×10^{-1}	1.50×10^{-1}
	S (psu)	5.60×10^{-3}	2.00×10^{-3}	9.90×10^{-3}	1.27×10^{-2}
	γ^n (kg m^{-3})	5.59×10^{-2}	7.30×10^{-3}	4.37×10^{-2}	1.76×10^{-2}

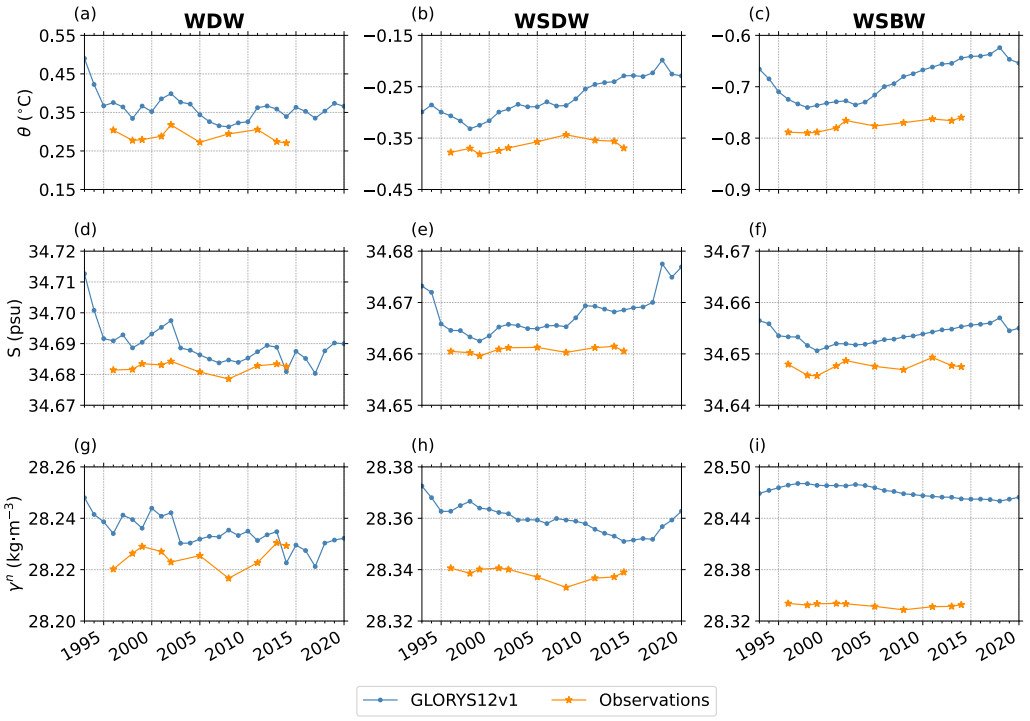

Figure 4: **Time series of annual average potential temperature (θ), salinity (S), and neutral density (γ^n) along Section A12 (1993–2020).** (a, b, c) θ (°C), (d, e, f) S (psu), and (g, h, i) γ^n (γ^n; kg m^{-3} for water masses layers defined by γ^n: WDW ($28.1 \leq \gamma^n < 28.27$ kg m^{-3}; a, d, g), WSDW ($28.27 \leq \gamma^n < 28.4$ kg m^{-3}; b, e, h), and WSBW ($\gamma^n \geq 28.4$ kg m^{-3}; c, f, i). GLORYS12v1 results (1993–2020) are shown as blue lines, and available observational data as orange lines.

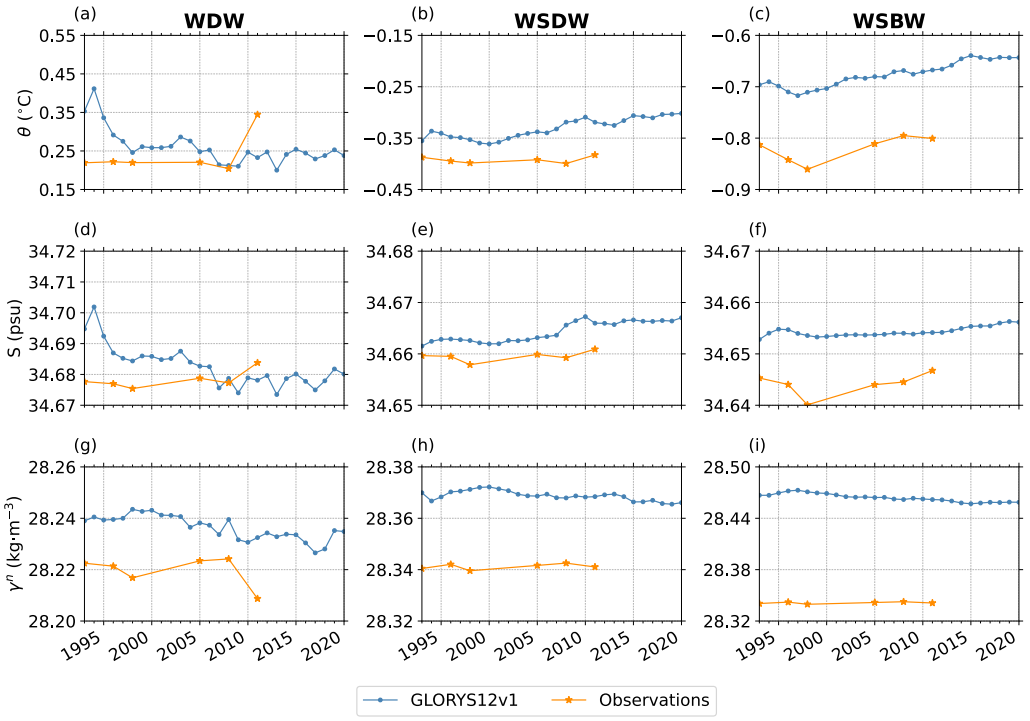

Figure 5: **Time series of annual average potential temperature (θ), salinity (S), and neutral density (γ^n) along Section SR4 (1993–2020).** (a, b, c) θ (°C), (d, e, f) S (psu), and (g, h, i) γ^n (γ^n; kg m^{-3} for water masses layers defined by γ^n: WDW ($28.1 \leq \gamma^n < 28.27$ kg m^{-3}; a, d, g), WSDW ($28.27 \leq \gamma^n < 28.4$ kg m^{-3}; b, e, h), and WSBW ($\gamma^n \geq 28.4$ kg m^{-3}; c, f, i). GLORYS12v1 results (1993–2020) are shown as blue lines, and available observational data as orange lines.

For the WSDW, the observations indicate a slight increase in θ in Section A12, while θ in Section SR4 and S in both sections remained relatively stable (Figures 4b,e and 5b,e). In contrast, GLORYS12v1 shows significant warming and salinification in both sections. In Section A12, θ increased at a rate of $4.3 \pm 0.4 \times 10^{-3}$ °C yr^{-1} (Figure 4b), and S increased at a rate of $3.8 \pm 0.5 \times 10^{-4}$ psu yr^{-1} (Figure 4e). In Section SR4, θ increased at a rate of $2.3 \pm 0.2 \times 10^{-3}$ °C yr^{-1} (Figure 5b), and S increased at a rate of $2.1 \pm 0.2 \times 10^{-4}$ psu yr^{-1} (Figure 5e). As a result of warming, the γ^n of the WSDW decreased at a rate of $-6.1 \pm 0.8 \times 10^{-4}$ kg m^{-3} yr^{-1} in Section A12 (Figure 4h) and $-1.9 \pm 0.3 \times 10^{-4}$ kg m^{-3} yr^{-1} in Section SR4 (Figure 5h).

For the WSBW, we observe larger differences between observations and GLORYS12v1 (Table 3). In both sections, observations suggest warming in the WSBW, although it is not as pronounced as in the reanalysis (Figures 4c and 5c). The observations indicate a stable S over time in Section A12, while in Section SR4, there is evidence of an increase in S after 1998 (Figures 4f and 5f, respectively). In the reanalysis, both sections show significant increasing trends in both θ and S. In Section A12, θ increases at a rate of $4.5 \pm 0.6 \times 10^{-3}$ °C yr^{-1} (Figure 4c) and S increases at a rate of $1.8 \pm 0.4 \times 10^{-4}$ psu yr^{-1} (Figure 4f). In Section SR4, θ increases at a rate of $2.9 \pm 0.2 \times 10^{-3}$ °C yr^{-1} (Figure 5c), and S increases at a rate of $8.0 \pm 1.4 \times 10^{-5}$ psu yr^{-1} (Figure 5f). Similarly to WSDW, the increase in θ results in a lighter WSBW by the end of the analyzed period. In Section A12, γ^n decreases at a rate of $-5.0 \pm 0.9 \times 10^{-4}$ kg m^{-3} yr^{-1} (Figure 4i) and $-5.3 \pm 0.4 \times 10^{-4}$ kg m^{-3} yr^{-1} (Figure 5i).

Due to the limited number of observations and irregular temporal spacing, it is not possible to calculate a robust observed trend that provides a meaningful error estimate, accurately reflecting the uncertainty associated with the reanalysis trend. Here, however, we compare the annual averages with the direct measurements available for the two sections (Table 2). Despite the differences, the RMSE values are generally lower than the corresponding standard deviation of the observed data, suggesting that the reanalysis can broadly reproduce observed variability, although some systematic biases remain. The exceptions are the S of the WSDW in Section A12 and the WSBW in both sections, which show RMSEs that are either close to or exceed the standard deviations.

3.3. Weddell Gyre Barotropic Streamfunction

We now assess the Weddell Gyre transport to investigate potential mechanisms contributing to the variability of the deep waters in the Weddell Sea

in GLORYS12v1. The mean state of the BSF reveals that the cyclonic Weddell Gyre extends further east to 80°E along the coastline (Figure 6a). The mean BSF (1993 to 2020) in the inner gyre ranges from 33.40 Sv to 48.71 Sv, which is in agreement with previous studies (e.g., Jullion et al., 2014; Reeve et al., 2019). Furthermore, GLORYS12v1 is capable of representing the double cell structure identified by Reeve et al. (2019), characterized by a stronger eastern cell and a weaker western cell.

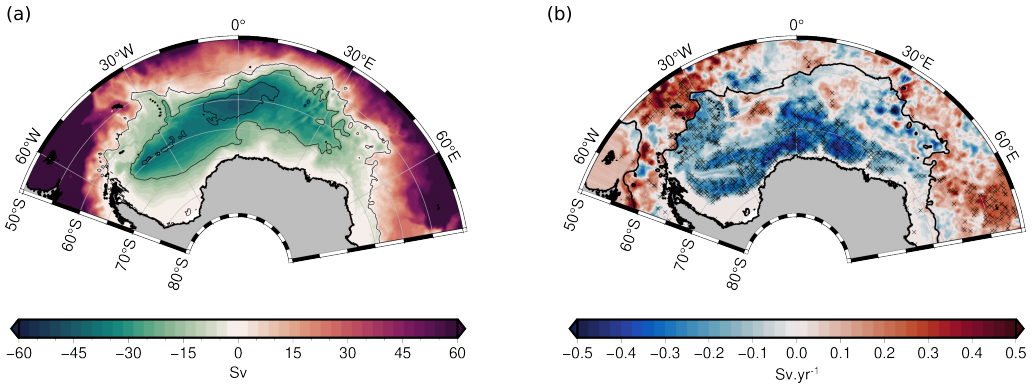

Figure 6: **Mean state and linear trends of the barotropic streamfunction (BSF) in the Weddell Sea (1993–2020).** (a) Mean BSF from GLORYS12v1. (b) Linear trends in BSF, with significant values (Mann–Kendall test, 95% confidence) marked by crosses. The contour in (b) denotes the zero BSF isoline, which separates the Weddell Gyre from the Antarctic Circumpolar Current.

The BSF trend reveals a general weakening of the Weddell Gyre, especially in the southern and western branches, with a rate of approximately -0.40 ± 0.03 Sv yr^{-1} (Figure 6b). This weakening in the Weddell Gyre may reduce the CDW inflow (see Discussion for more details; Ryan et al., 2016). Additionally, the southern branch of the Weddell Gyre is directly connected to coastal circulation and thus influences the transport and distribution of deep waters within and outside the Weddell Gyre. Therefore, changes in the gyre strength have the potential to drive changes in the deep water masses. This is investigated next.

The complex MCA results show that mode 1 explains more than 90% of the squared covariance fraction for both θ (Figure 7) and S (Figure 8) across all water mass layers. The spatial patterns of the amplitude of covariance (Figures 7a–f and 8a–f) reveal strong coupling between the BSF and the

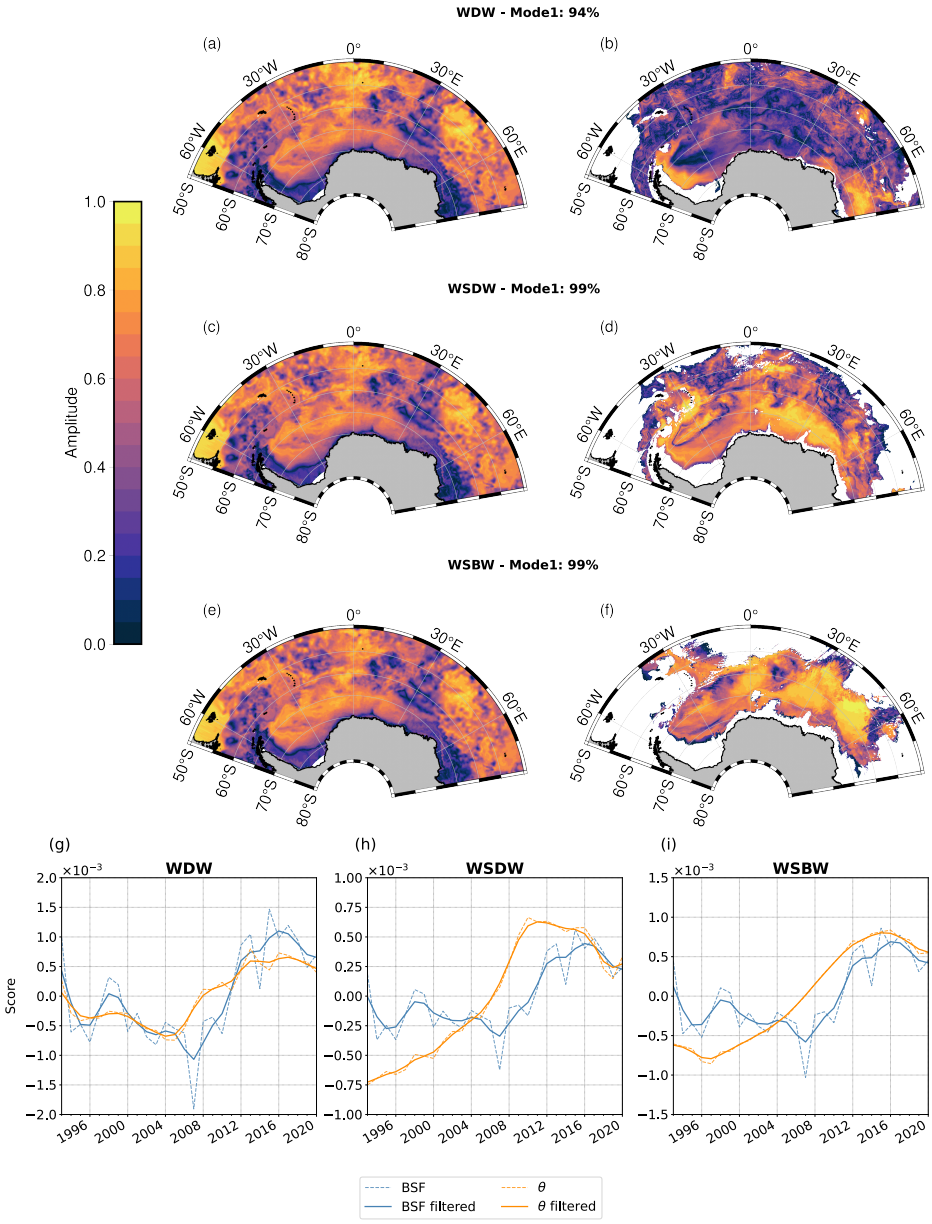

Figure 7: **Leading mode of covariability between the barotropic streamfunction (BSF) and potential temperature (θ).** Amplitudes of covariance associated with mode 1 between BSF (a, c, and e) and θ of the WDW (b), WSDW (d), and WSBW (f) layers. The corresponding scores (g–i) are plotted, showing only the real part, illustrating the temporal variation of mode 1 between BSF and potential temperature. In the spatial patterns, more yellowish tones indicate larger amplitudes of covariability.

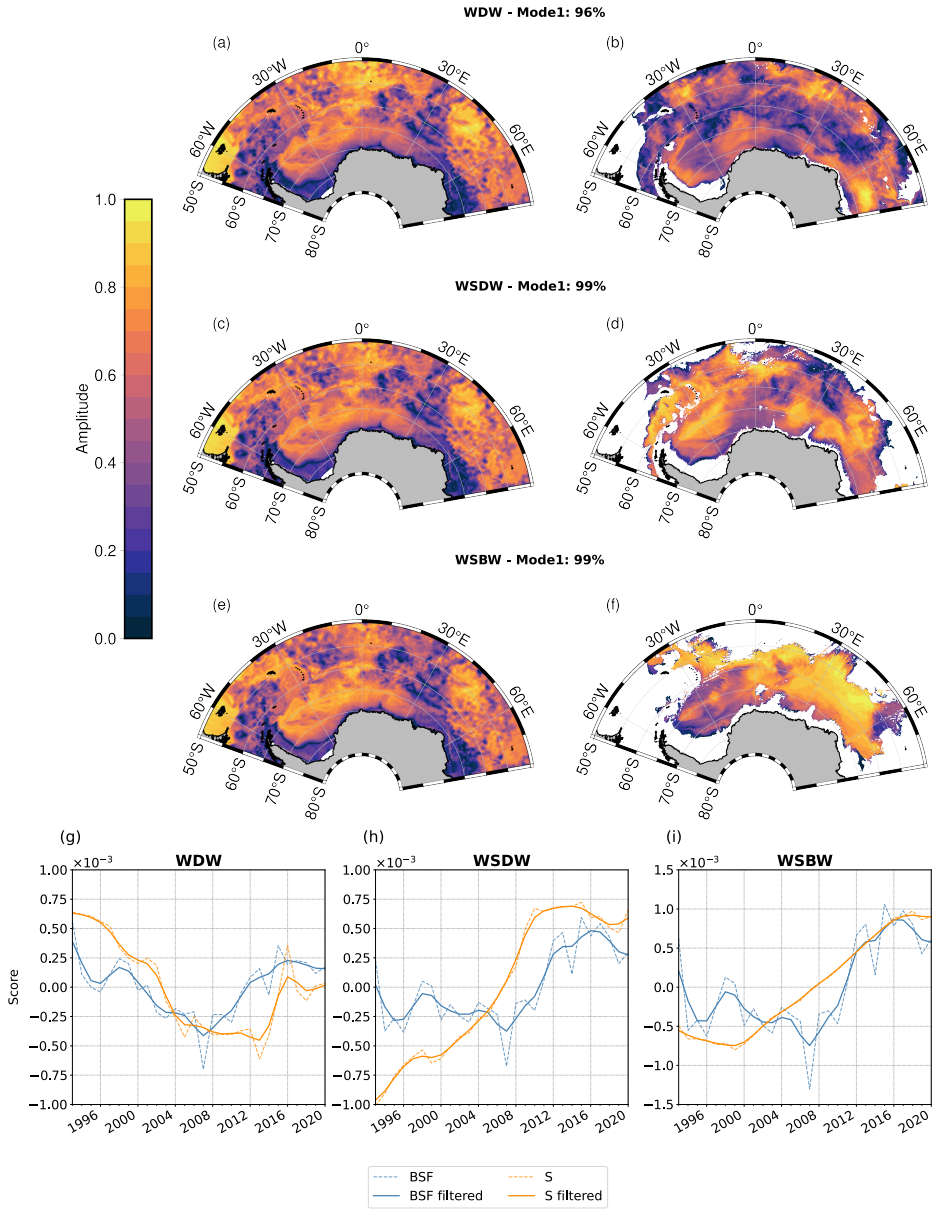

Figure 8: **Leading mode of covariability between the barotropic streamfunction (BSF) and salinity.** Amplitudes of covariance associated with mode 1 between BSF (a, c, and e) and θ of the WDW (b), WSDW (d), and WSBW (f) layers. The corresponding scores (g–i) are plotted, showing only the real part, illustrating the temporal variation of mode 1 between BSF and potential temperature. In the spatial patterns, more yellowish tones indicate larger amplitudes of covariability.

hydrographic properties of the water masses, while the temporal evolution of the complex MCA mode 1 scores (Figures 7g–i and 8g–i) indicates coherent decadal variability between BSF and hydrographic properties in each layer.

For the WDW, large amplitudes of covariability occur in the southern Weddell Sea (Figures 7b and 8b). For θ (Figure 7b), these amplitudes are restricted to the southwestern and southeastern Weddell Sea, particularly near the coastal regions, with small amplitudes observed between 0° and 30°E. In contrast, S amplitudes follow the southwestward flow within the gyre (Figure 8b). While S variability is largely in phase with variations in BSF (indicated by similar colors or values close to zero; Figure B.2b), θ variations in the region with smaller amplitudes precede changes in BSF by 3 to 6 months (between $\pi/2$ and π; Figure B.1b). This suggests that other processes might first alter the thermohaline properties of the WDW, with these changes subsequently influencing, or being reflected in, adjustments to the gyre's barotropic structure.

In contrast, for the WSDW (Figures 7d and 8d) and WSBW (Figures 7f and 8f), large amplitudes are observed throughout the entire domain. Although the analysis of the phase between BSF and the hydrographic properties of these two water masses shows that they are largely in phase with variations in BSF, they also show an out of phase area west of 10°E, for both deep waters θ (Figures B.1d and B.1f), and for WSDW S (Figure B.2d). This result indicates that changes in these two water masses occur 3 to 6 months before changes in the circulation.

3.4. External Forcings

To evaluate the influence of external forcings on water mass variability, we analyzed the covariability between their properties and both wind stress curl and SIC. The BSF, which is closely coupled with atmospheric forcing, revealed a dominant mode of covariability (mode 1: 96%), characterized by interannual to decadal variability in the Weddell Gyre (Figure B.4). The complex MCA between the wind stress curl and the properties of the water masses shows that the former has large spatial amplitudes of covariability consistent with the cyclonic feature centered at 30°E (Figure 9a). While the WSDW and WSBW show broad covariability patterns across the Weddell Sea in mode 1 (explaining over 80% of covariance), similar to the patterns found between BSF and hydrographic properties in the previous section (Figures B.5 and B.6), the WDW shows significant amplitudes of covariability in mode 2. This mode explains 35% of the covariance with θ and 24% with S

in the southwestern Weddell Sea (Figure 10b,d), where small amplitudes of covariability are found between BSF and WDW θ (Figure 7b).

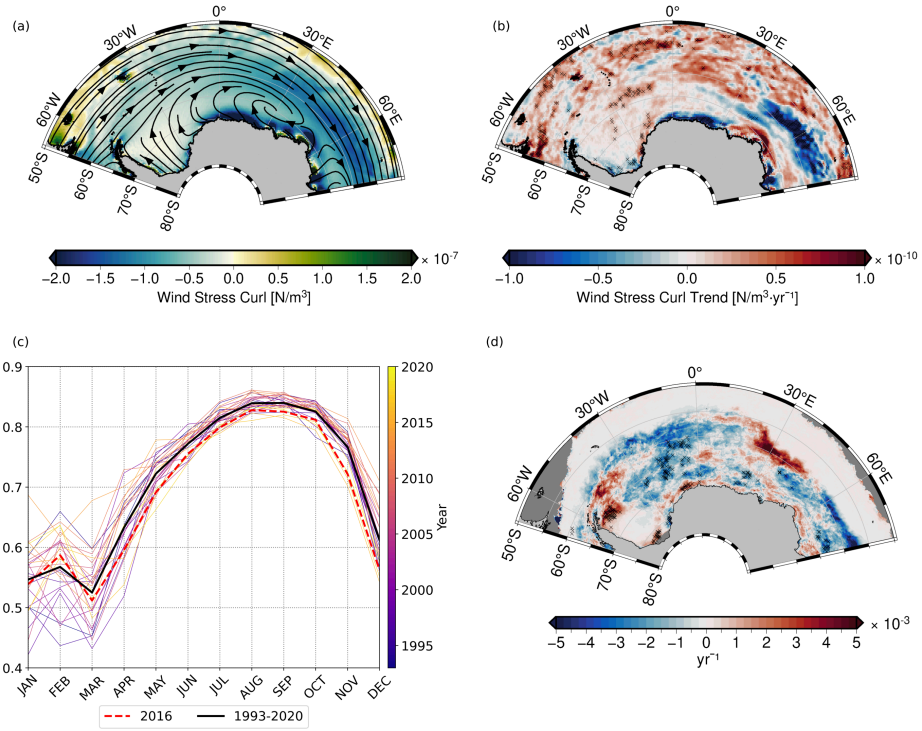

Figure 9: **Mean state and linear trends of wind stress curl and sea ice concentration (1993–2020).**(a) Mean ERA5 wind stress curl with black streamlines indicating surface circulation. (b) Trends in wind stress curl, calculated using absolute values. (c) Seasonal cycle of SIC calculated for each year. The black solid line represents the seasonal cycle for the entire period, while the dashed red line corresponds to 2016. (d) Trends in SIC. Statistically significant trends, determined using the Mann-Kendall test, are marked with crosses at the 95% confidence level.

These results suggest that the variability of the properties of the deep and bottom water masses is more strongly influenced by coupled wind-driven barotropic circulation. In contrast, WDW variability appears to be more closely related to regional wind stress curl within the gyre, highlighting the role of wind-driven Ekman pumping. The associated scores indicate a decadal variability in the relationship between wind stress curl and WDW θ and S (Figure 10d,e). Additionally, the phase analysis indicates that while variations in S in the inner Weddell Sea are in phase with wind stress curl, θ has

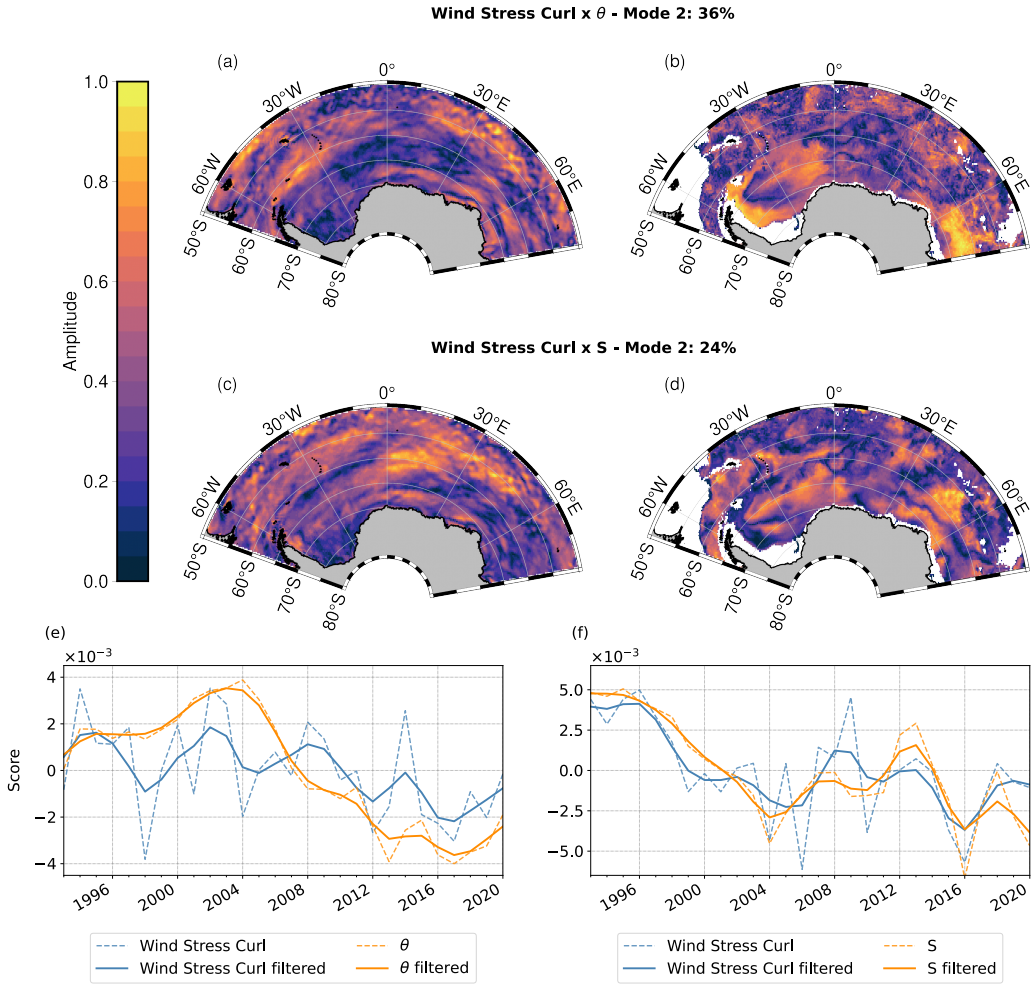

Figure 10: **Second mode of covariability between wind stress curl and WDW hydrographic properties.** Amplitudes of covariance associated with mode 2 between the wind stress curl (a, c) and WDW potential temperature (θ) (b) and salinity (d). The corresponding scores (e, f) are plotted, showing only the real part, illustrating the temporal variation associated with mode 2 between the wind stress curl and WDW θ (e) and salinity (f). In the spatial patterns, more yellowish tones indicate larger amplitudes of covariability.

a lag of approximately 3 months ($-\pi/2$; Figure B.3).

SIC in GLORYS12v1 reproduces the seasonal cycle reasonably well, despite the spread in February, and captures the sea ice decline observed after 2016 (Figure 9c). In GLORYS12v1, the SIC increased in the northeastern region of the Weddell Sea, around 30°E, and near the northern tip of the Antarctic Peninsula. A significant decrease in SIC is observed in the central area, west of the Greenwich Meridian (Figure 9d).

To analyze the influence of SIC on the deep water masses, we considered only grid cells where SIC was greater than 15%. For all three water masses, the complex MCA mode 1 is characterized by high amplitudes of SIC variability in the southwestern Weddell Sea, along the continental slope and shelf break, regions of persistent sea ice coverage (see Figure D.1), and areas where significant SIC trends are observed (Figure 9d). For both the WSDW and WSBW, this leading mode explains more than 90% of the covariance with SIC. Mode 1 shows a broad covariability pattern that aligns with a gyre-scale adjustment of hydrographic properties (Figures 13 and 14). Phase analysis (not shown) indicates that WSBW responds directly to SIC variability, whereas WSDW shows a phase relationship similar to that between BSF and WSDW (Figures B.1d and B.2d). These results support the interpretation that the coupled dynamics of the gyre circulation and fluctuations in wind stress curl and SIC modulate the variability of WSDW and WSBW. This coupling gives rise to the decadal variability observed in the hydrographic properties of these two deep water masses.

In contrast, mode 1 explains 60% of the covariability between SIC and WDW θ, and 71% of the covariability between SIC and WDW S. For both mode 1, high amplitudes are observed in the northeastern and southwestern sectors, near regions of strong SIC variability. However, for S, the strongest amplitudes are concentrated in the northern, central, and eastern portions of the area. Additionally, in this mode, θ exhibits signs of a decadal adjustment, whereas S displays a multiyear variability pattern. Mode 2 also emerges as significant, capturing 26% and 19% of the SIC covariability with WDW θ and S, respectively. Spatially, mode 2 shows enhanced amplitudes of covariability in offshore regions, where the seasonal cycle of sea ice advance and retreat is strongest (Figure D.1). This result suggests that mode 2 captures a seasonally driven mode of SIC–WDW interaction. In mode 2, θ exhibits a broader spatial pattern of variability, whereas S displays a more localized structure, particularly in the eastern sector. In this mode, both hydrographic properties appear to be associated with a long-term response to

SIC variability. Phase analysis between SIC and WDW hydrographic properties (not shown) reveals that S variations are largely in phase with regions of strong SIC variability, while θ exhibits a phase relationship similar to that between BSF and WDW (Figure B.1b), indicating that θ changes in WDW precede circulation changes by 3 to 6 months.

4. Discussion and conclusions

In this study, we assessed the representation and variability of WDW, WSDW, and WSBW in the Weddell Sea using the GLORYS12v1 reanalysis, with a focus on the long-term repeat hydrography sections A12 and SR4. Although GLORYS12v1 captures key features of hydrographic structure and variability, biases in S trends and in deeper layers highlight important limitations. We first examine the vertical structure of water masses, followed by their temporal variability and the underlying atmospheric and sea ice drivers. Although the upper ocean is not the primary focus, we discuss its biases due to their potential to influence deeper layers through vertical processes.

4.1. Representation of Water Column Structure

GLORYS12v1 reproduces the general vertical structure of the Weddell Sea water masses; however, we found large biases in the upper layer, consistent with the global assessment of GLORYS12v1 by Drévillon et al. (2022b). In the regional context of the Weddell Sea, surface θ and S biases exceed the global averages reported by Drévillon et al. (2022b), particularly for θ, with errors extending down to 400 m well below the 100 m depth threshold seen globally.

The failure to reproduce near-surface features, such as the remnant Winter Water layer, a hallmark of Antarctic spring/summer conditions, likely contributes to the upper-layer discrepancies. Despite these surface limitations, comparisons with WOA18 indicate that the intermediate layer (300–2000 m) is reasonably well represented. GLORYS12v1 also successfully captures the cold bottom layer (temperatures < -0.7°C) characteristic of WSBW, which is absent in WOA18.

4.2. Temporal Variability of the Deep Water Masses

Our analysis revealed that GLORYS12v1 is generally colder than WOA18 in the intermediate and deep layers, considering the time-mean structure. However, GLORYS12v1 is warmer and saltier than observations across all

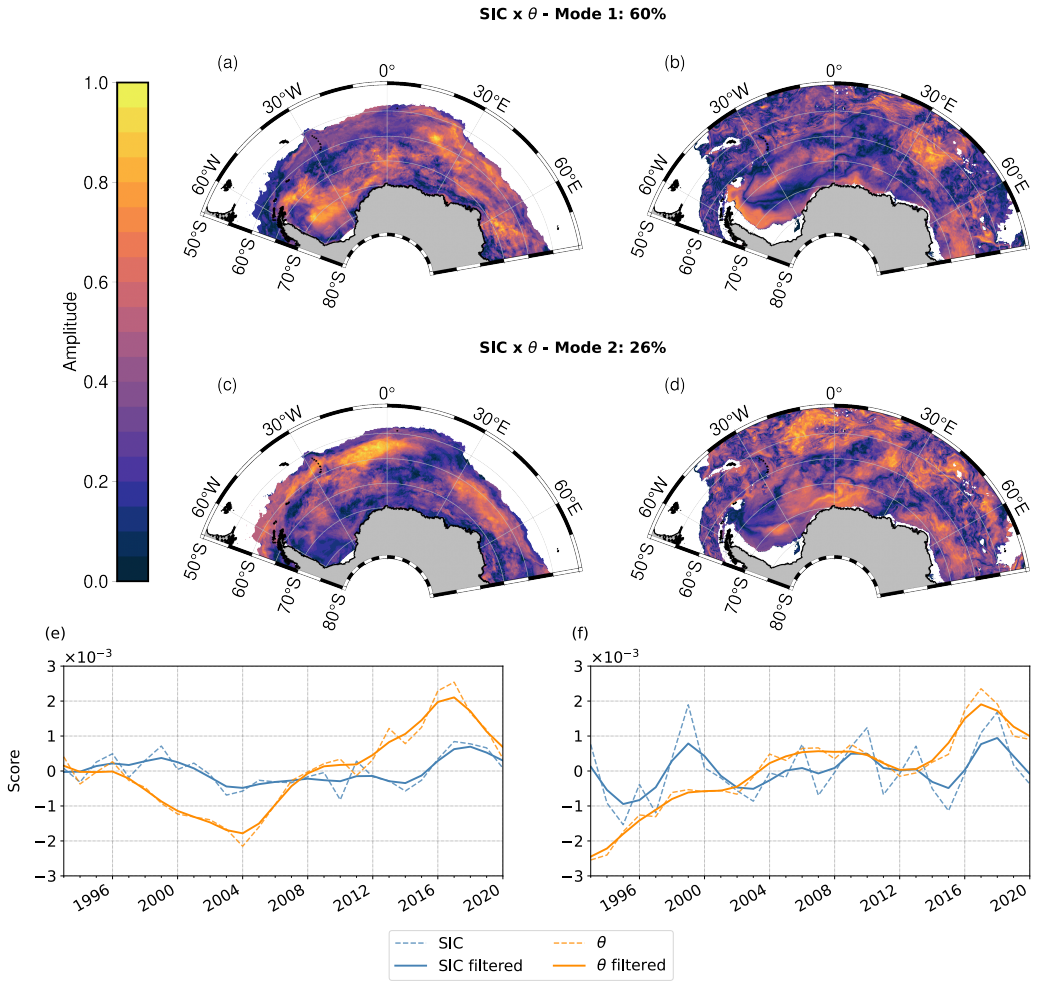

Figure 11: **First and second modes of covariability between sea ice concentration (SIC) and WDW potential temperature (θ).** Amplitudes of covariance between SIC and WDW θ associated with mode 1 (a, b) and mode 2 (b, c). The corresponding scores are plotted, showing only the real part, illustrating the temporal variation associated with mode 1 (e) and mode 2 (f). In the spatial patterns, more yellowish tones indicate larger amplitudes of covariability.

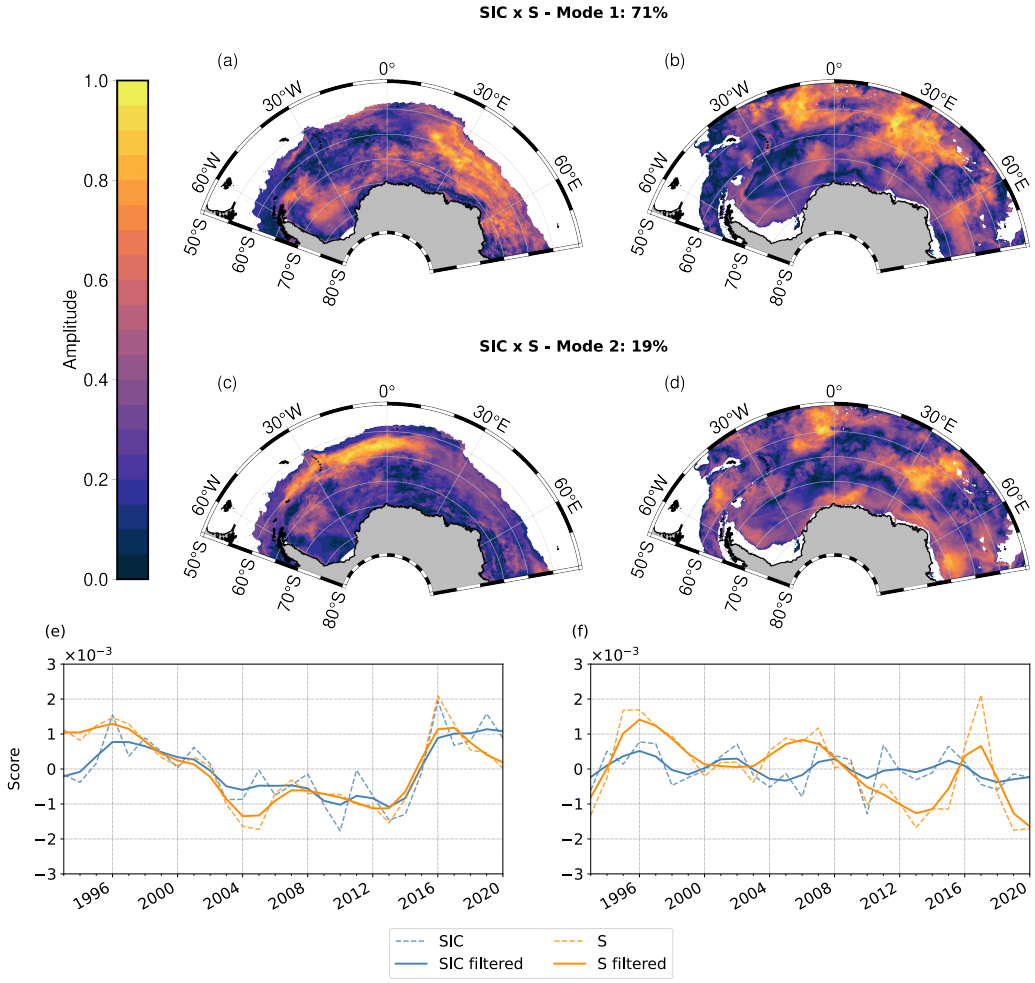

Figure 12: **First and second modes of covariability between sea ice concentration (SIC) and WDW salinity.** Amplitudes of covariance between SIC and WDW salinity associated with mode 1 (a, b) and mode 2 (b, c). The corresponding scores are plotted, showing only the real part, illustrating the temporal variation associated with mode 1 (e) and mode 2 (f). In the spatial patterns, more yellowish tones indicate larger amplitudes of covariability.

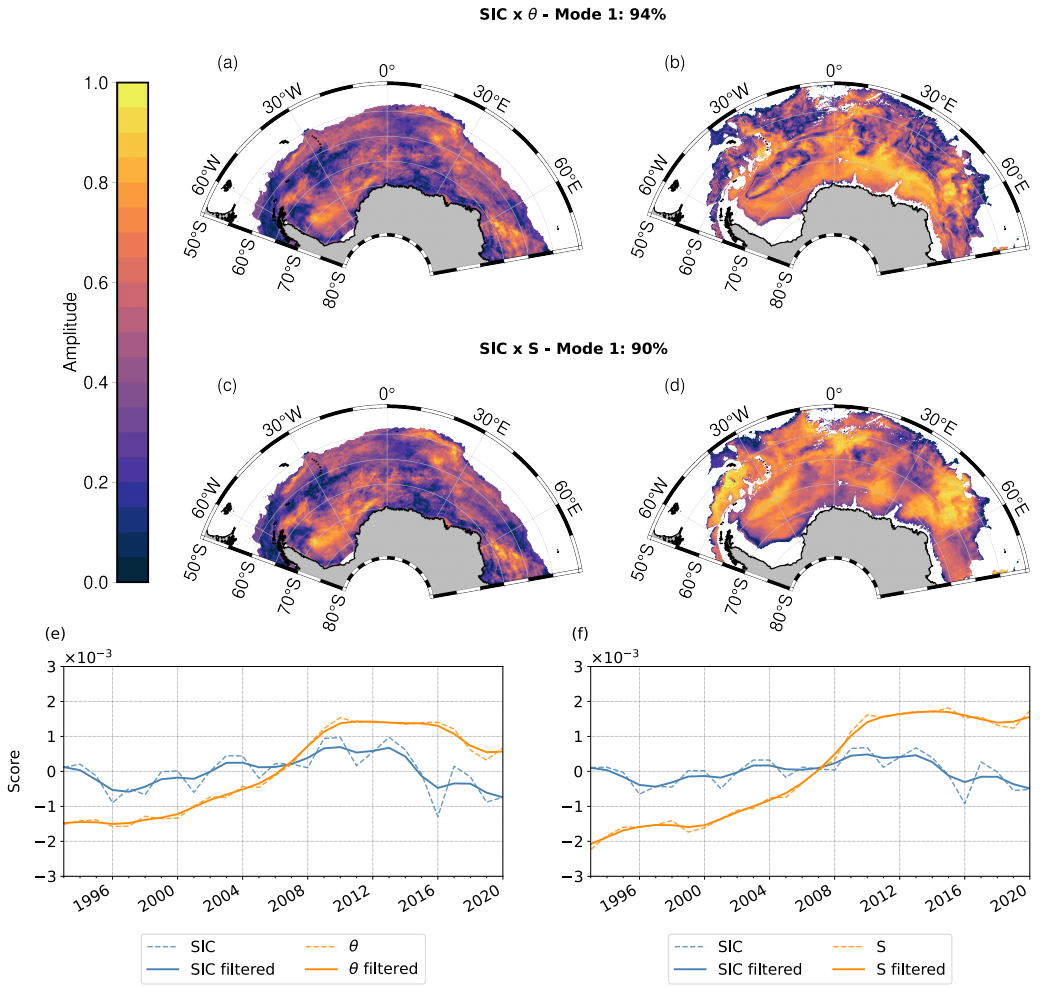

Figure 13: **Leading mode of covariability between sea ice concentration (SIC) and WSDW hydrographic properties.** Amplitudes of covariance associated with mode 1 between the SIC (a, c) and WSDW potential temperature (θ) (b) and salinity (d). The corresponding scores are plotted, showing only the real part, illustrating the temporal variation associated with mode 1 between the SIC and WSDW θ (e) and salinity (f). In the spatial patterns, more yellowish tones indicate larger amplitudes of covariability.

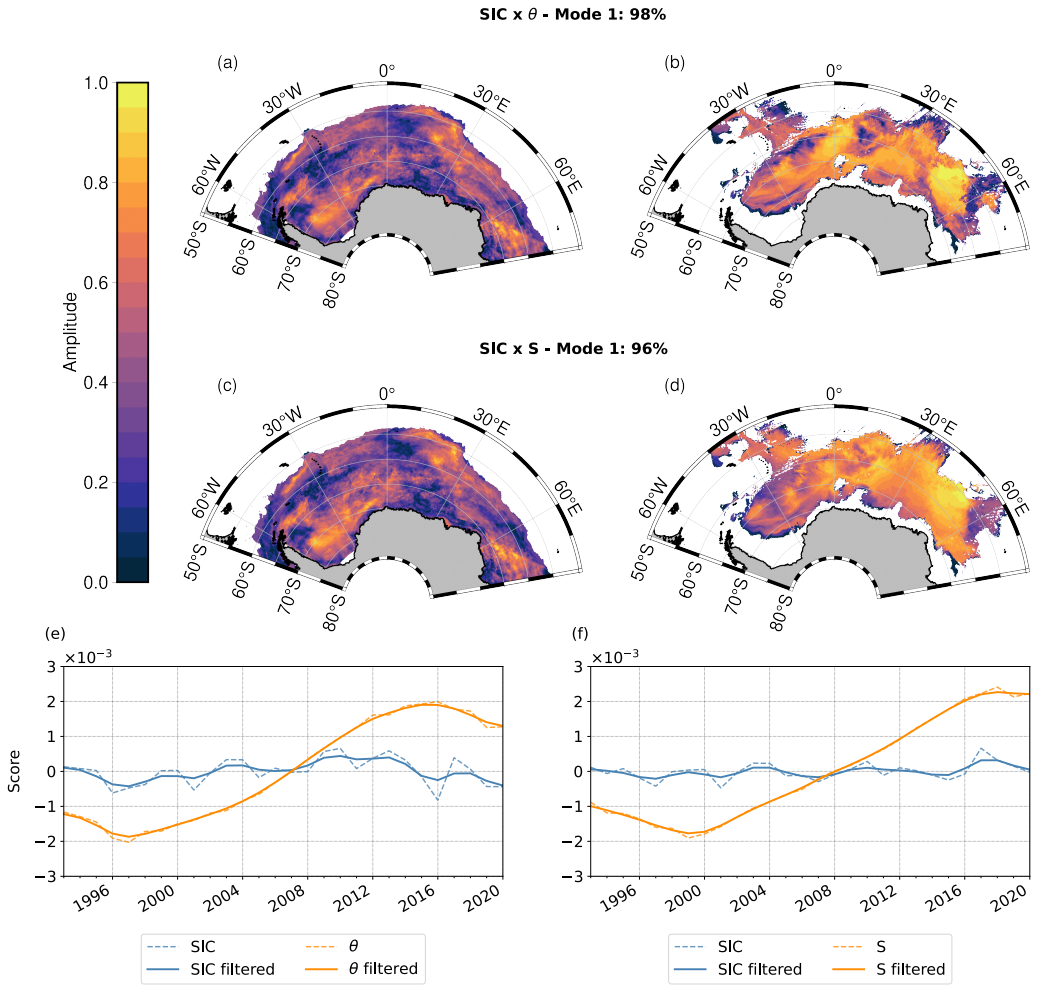

Figure 14: **Leading mode of covariability between sea ice concentration (SIC) and WSBW hydrographic properties.** Amplitudes of covariance associated with mode 1 between the SIC (a, c) and WSBW potential temperature (θ) (b) and salinity (d). The corresponding scores are plotted, showing only the real part, illustrating the temporal variation associated with mode 1 between the SIC and WSBW θ (e) and salinity (f). In the spatial patterns, more yellowish tones indicate larger amplitudes of covariability.

three water masses along sections A12 and SR4. This contrast highlights the uncertainty introduced by sparse observations in the region. WOA18, which is an objectively analyzed product, is highly interpolated in data-poor regions, such as the Weddell Sea, which can limit its reliability. In contrast, long-term hydrography sections are limited in temporal and spatial coverage, primarily capturing austral summer conditions. Therefore, we treat the hydrography sections as the primary benchmark for validating absolute water mass properties, while WOA18 provides a broader climatological frame of reference. These complementary comparisons underscore the challenges of evaluating the accuracy of reanalysis in high-latitude oceans, where observational constraints remain a significant limitation.

In this study, we did not estimate long-term trends directly from the observational data due to their limited number and irregular temporal distribution. However, Strass et al. (2020) provide a valuable long-term perspective based on repeated hydrographic sections collected in the deep Weddell Sea between 1989 and 2019. Their work introduces an alternative methodological approach, in which estimated long-term trends are superimposed onto the mean vertical profiles to reconstruct spatial patterns of change over time. This technique allowed the authors to represent the evolution of water mass properties between the start and end of their observational period, capturing multi-year trends at different depth layers. Their results showed no significant long-term temperature trend in the upper 700 m, although they observed a clear trend of freshening in that layer. In contrast, waters below 700 m exhibited marked warming and salinification, which aligns qualitatively with the trends captured by GLORYS12v1. A direct comparison between the two studies, however, is limited by differences in methodology and temporal coverage. Strass et al. (2020) analyzed a more extended period, starting in 1989, and used a distinct framework to define vertical layers. Nevertheless, using the isopycnals displayed in Figure A.1, we can approximate a correspondence between the water masses analyzed here and their vertical bins: our WDW layer (500–2000 m) overlaps with their 700–2000 m range, WSDW with the 2000–4000 m layer, and WSBW with depths below 4000 m.

Within this broader context, our results for WDW diverge from those of Strass et al. (2020), who found warming in the 700–2000 m range, whereas GLORYS12v1 shows no trend in θ but a freshening trend. Still, it is worth noting that freshening was also reported above 700 m in their study (see Table 4 in Strass et al., 2020), which may partially reconcile these differences. For WSDW and WSBW, both datasets consistently indicate warm-

ing and increased salinity. Yet, GLORYS12v1 tends to overestimate the magnitude of temperature and salinity changes, especially in Section A12. In GLORYS12v1, WSDW θ and S trends exceed observations by up to $+2.4 \times 10^{-3}$ °C yr^{-1} and $+3.4 \times 10^{-4}$ psu yr^{-1}, respectively. In WSBW, the largest temperature bias also occurs in Section A12 ($+2.4 \times 10^{-3}$ °C yr^{-1}), while salinity trends exceed the observed values by $+1.3 \times 10^{-4}$ psu yr^{-1}.

As a result of the more pronounced warming, γ^n trends in GLORYS12v1 are also generally more negative, particularly in Section A12. Still, both observations and reanalysis indicate that WSDW and WSBW are becoming less dense, primarily due to increasing temperature. According to Strass et al. (2020), the mean heating rate for layers below 2000 m exceeds the global ocean average by a factor of about five. This trend underscores the importance of ongoing monitoring of this region, as WSDW and WSBW are precursors of AABW, and changes in these deep-water masses may have far-reaching implications for the global abyssal ocean (Li et al., 2023; Zhou et al., 2023).

4.3. Drivers of Hydrographic Variability

The variability of Weddell Sea deep waters in GLORYS12v1 appears to result from multiple combined factors, including coupled variability between the Weddell Gyre, wind stress, and SIC. It is well established that the Weddell Gyre is primarily wind-driven. This is well captured by GLORYS12v1, which shows a strong coupling between the BSF and the wind stress curl (Figure B.4). Still, the gyre's response to wind forcing is not symmetric.

According to Fahrbach et al. (2011) and Armitage et al. (2018), strengthening westerlies tend to intensify the eastward flow in the northern limb of the gyre while weakening the westward return flow in the southern branch. This asymmetric response is partially evident in the GLORYS12v1 long-term trends. Wind stress curl trends are strongest along the northern boundary of the gyre (Figure 9b), where they reflect the intensification of the westerlies. Despite this, the northern limb of the gyre exhibits predominantly weakening BSF trends (Figure 6b). In contrast, the weakening of the Weddell Gyre circulation is most pronounced along the southern branch, where it aligns with negative trends associated with easterly winds over the coastal region (Figures 6b and 9b). Although trends do not suggest a straightforward response to wind forcing along the northern boundary, this divergence may be explained by (i) delayed or non-linear ocean response, (ii) changes in stratification, and (iii) effects of eddy saturation in the Antarctic Circumpolar

Current region that limit flow increases despite stronger winds (Hogg et al., 2015; Wainer and Gent, 2019).

Weakened gyre strength in the southern and western branches may limit the eastward inflow of CDW and export of AABW. According to Ryan et al. (2016), the southern branch is part of an advective pathway of CDW into the eastern Weddell Sea boundary, and the variability can be connected to changes in the regional wind field. Furthermore, a weak western boundary of the gyre likely results in reduced export of these water masses, leading to longer residence times within the Weddell Sea and thereby enhancing their exposure to buoyancy forces. This exposure promotes the cooling and freshening of WDW by reducing the inflow of warm, salty CDW and amplifying surface-driven changes through prolonged ocean–ice–atmosphere interactions, explaining the WDW cool bias in Section SR4 (Figure 5a). Further supporting the residence-time hypothesis, WDW θ and S covaried strongly with wind stress curl in the southeastern and southwestern gyre, where cyclonic features dominate (Figure 9a). Strengthening westerlies in these regions drives enhanced Ekman transport, promoting upwelling, which reinforces the cooling in Section SR4 (Figure 5a).

Our results show a strong decadal-scale coupling between BSF and the hydrographic properties across all water masses. The properties of WDW, WSDW, and WSBW show a broad spatial covariability with the gyre transport. On the other hand, WDW θ covaries most strongly along the coast, especially near the southeastern Weddell Sea and Antarctic Peninsula. Here, weakening the northward outflow contrasts with relative stability in the eastern inflow, reinforcing the asymmetric gyre response.

In addition to wind-driven effects, SIC is also a key factor associated with the variability of the Weddell Sea water masses. Sea ice formation and brine rejection are likely strong in areas of high SIC variability, explained by mode 1. In ocean reanalyses and Oceanic General Circulation Models, the primary mechanism for deep and bottom water formation often relies on unrealistic deep convection, which is a frequent source of error in the representation of AABW (Azaneu et al., 2014; Aguiar et al., 2017; Heuzé, 2021; Mohrmann et al., 2021). This artificial convective process can disrupt the stratification of the water column, leading to the sinking of warmer and saltier waters and contributing to the observed warming and salinification trends in the WSDW and WSBW layers.

In coupled models, deep convection can drive decadal to multidecadal variability in the sea ice area, limiting the influence of wind stress, unlike

observations, where wind stress plays a dominant role (Behrens et al., 2016). This sea ice variability has, in turn, been linked to decadal variations in the strength of the Weddell Gyre, suggesting a link between deep convection and regional ocean circulation (Behrens et al., 2016), which is consistent with our results.

In summary, Weddell Sea water mass variability in GLORYS12v1 reflects a complex interplay between atmospheric forcing, gyre circulation, and sea ice dynamics. WSDW and WSBW are strongly modulated by decadal-scale variability driven by the coupled atmosphere–ocean–ice system. Their broad covariability with both BSF and SIC suggests that changes in wind stress curl and sea ice formation jointly modulate deep convection and the redistribution of water mass properties. The prominence of mode 1 in the complex MCA, with SIC accounting for over 90% of the variability for both WSDW and WSBW, highlights the strong control of sea ice conditions over bottom water formation and transformation processes. Phase analysis indicates that WSBW responds more directly to SIC variability, while WSDW exhibits a phase-lagged response, consistent with modulation by changes in gyre strength. These patterns support a physical mechanism in which sea ice variability alters brine rejection and stratification, which, in turn, regulates deep convection and influences deep water mass properties.

WDW shows more complex behavior, characterized by multiple modes of covariability and phase relationships that distinguish its response from that of deeper layers. WDW S is largely in phase with BSF and SIC variability. However, while the covariability with BSF is stronger along the southwestward gyre path, suggesting that its salinity is primarily governed by lateral advection and mixing within the gyre, the covariability with SIC is more localized and likely reflects the influence of deep convection on intermediate depths. In contrast, WDW θ tends to lead both BSF and SIC changes by 3 to 6 months, pointing to a preceding atmospheric forcing mechanism. This result suggests that WDW thermohaline properties are first altered by changes in wind-driven Ekman transport and surface fluxes, especially in the coastal southwestern and southeastern Weddell Sea, before being integrated into the larger-scale circulation. A secondary SIC–WDW mode, with offshore expression, reflects seasonal sea ice variability and may capture the response of WDW to longer-term trends in sea ice advance and retreat, further reinforcing the role of residence time and delayed mixing in shaping WDW evolution.

4.4. Implications and Limitations

The eddy-permitting reanalysis Southern Ocean State Estimate (SOSE; Mazloff et al., 2010) has been widely used and validated to investigate circumpolar circulation and water mass transformation (e.g., Cerovečki et al., 2013; van Sebille et al., 2013; Abernathey et al., 2016; Narayanan et al., 2023). SOSE provides an ocean climate baseline through an adjoint-based assimilation framework, which ensures dynamical consistency and allows observational information to be propagated across variables through model physics, yielding better agreement with observations than objectively analyzed climatologies such as WOA (Mazloff et al., 2010; Verdy, A. and Mazloff, M. R., 2017). Still, the sparse observational coverage and the limited representation of small-scale processes remain a constraint for SOSE, meaning that some physical features may still be underrepresented. In this context, GLORYS12v1 emerges as a potential tool, improving resolution and providing reconstruction over a more extended period than SOSE. Lellouche et al. (2021) provide an extensive validation of GLORYS12v1 and highlight its realistic representation of major oceanic features, including sea level variability and mesoscale activity, being a valuable tool for studying large-scale ocean circulation. However, while GLORYS12v1 can provide meaningful insights into broader gyre dynamics, it is less suited for investigating regions like the Weddell Sea, where fine-scale processes play a critical role.

As highlighted by Lellouche et al. (2021), the assimilation of observational data significantly improves reanalysis accuracy, evidenced by the reduction in temperature and salinity biases following the deployment of the global Argo array in 2004. Yet, in data-sparse regions like the Weddell Sea, the absence of sustained observations, especially at depth and near the coast, limits the ability of reanalysis systems to accurately represent water mass properties. The continued evolution of observing systems, including high-resolution satellite missions for sea-ice covered regions (Dotto et al., 2018; Armitage et al., 2018; Naveira Garabato et al., 2019) and deep ocean profiling through Deep Argo (Johnson et al., 2015; Jayne et al., 2017), will be essential for reducing uncertainties and improving the fidelity of reanalysis products in polar regions. Deeper water masses exhibit long-term variability on interannual to decadal timescales. Therefore, alongside the expansion of observational capabilities, sustained numerical efforts to improve the representation of physical processes, particularly those governing deep and bottom water formation, remain essential for accurately capturing their evolution.

Despite its high resolution, the system configuration used in GLORYS12v1

still struggles to accurately capture regional processes in the Weddell Sea. It also retains some biases found in SOSE, such as pronounced warming and salinification, as well as the lack of representation of coastal dynamics, which prevents these reanalyses from capturing dense shelf waters and AABW formation (Nakayama et al., 2024). GLORYS12v1 does not fully resolve the mesoscale eddy field in this region, where the Rossby radius is approximately 4 km, which requires a horizontal grid resolution of at least 1 km (Nøst et al., 2011; Hattermann et al., 2014; Thompson et al., 2014). These unresolved scales are critical for capturing eddy-driven exchange across the continental slope and within the gyre.

The observed covariance patterns and their vertical extent suggest the influence of deep convection on water mass transformation processes in GLORYS12v1, particularly linking SIC variability to subsurface water mass properties at depths below 500 m. Our hypothesis is reinforced by other limitations in the GLORYS12v1 system, such as (i) a poor representation of interior mixing, since tides are not explicitly resolved and mixing is represented with spatially constant diffusivity, (ii) ice shelf cavities are not included, and (iii) use z-level vertical coordinate (Lellouche et al., 2018; Oelerich et al., 2022).

The absence of ice shelf cavity and unresolved submesoscale features leads to an unrealistic representation of DSW and the circulation within the ice shelf cavities, thus affecting the representation of water mass transformation (Stewart et al., 2019; Oelerich et al., 2022). Several studies have shown that both tides and meso- and submesoscale eddies play an essential role in cross-slope exchanges and mixing along the Antarctic margins (Daae et al., 2009; Nøst et al., 2011; Thompson et al., 2014; Hattermann et al., 2014; Flexas et al., 2015; Stewart et al., 2019).

Due to the step-like bottom topography, along with poorly represented interior mixing, the vertical z-level coordinate generally overestimates the vertical mixing (Lellouche et al., 2018). In regions of dense overflow, such as the Southwestern Weddell Sea, the dense plume remains near the coast, failing to cascade downslope (Ezer and Mellor, 2004). This misrepresentation is particularly critical along the Antarctic margins, especially in locations where AABW is formed, as the eddy overturning is also modulated by topography (Thompson et al., 2014; Daae et al., 2017). Therefore, the limitations in GLORYS12v1 directly affect coastal processes related to the formation of WSDW and WSBW.

The underrepresentation of coastal processes not only hampers the accurate depiction of deep water mass formation but also directly impacts the

southern and western branches of the Weddell Gyre, which are closely connected to coastal circulation. Neme et al. (2021) showed that increasing resolution leads to a more unstable Weddell Gyre and an eastward extension of the cyclonic flow. While GLORYS12v1 indicates this eastward expansion, it does not show a significant change in the magnitude of barotropic transport relative to the lower-resolution run (GLORYS2V4; Figure C.1). This discrepancy likely reflects the underrepresentation of coastal fluxes in the reanalysis, which may contribute to the biases in simulating deep water variability in the Weddell Sea.

Although GLORYS12v1 combines numerical modeling improvements with data assimilation, limitations in resolving key processes and the scarcity of observations in the Weddell Sea, especially at deeper layers, remain significant challenges. Previous studies suggest potential improvements that could enhance the representation of deeper layers, such as increasing both horizontal and vertical resolution and implementing more sophisticated vertical coordinate systems, such as z^*, which would improve topographic representation and allow better simulation of DSW and its associated dense overflow (Morrison et al., 2020; Neme et al., 2021). Another approach is the implementation of the overflow parameterization, as demonstrated by Danabasoglu et al. (2020), which showed better representation of AABW compared to other models in the Phase 6 of the Coupled Model Intercomparison Project (Heuzé, 2021).

It is worth mentioning that we previously compared GLORYS12v1 and EN4 (not shown), and we found a bias in salinity in 2018 in Section A12. Since GLORYS12v1 is initialized by EN4, this outlier can likely affect GLORYS12v1 results for the region. Therefore, we recommend that in future studies using GLORYS12v1 outputs, users must be cautious with data from 2018 onwards, and may consider excluding this period.

Finally, our findings highlight the need for ongoing advancements in data acquisition and numerical simulations, highlighting that improving horizontal resolution alone is insufficient to enhance the representation of the Weddell Sea. Instead, improvements in the vertical coordinate scheme or the implementation of parameterized Antarctic shelf processes are necessary to better represent overflows, along with enhanced eddy parameterization to reduce non-physical mixing processes. These improvements are crucial for accurately representing Antarctic coastal processes related to AABW formation. Understanding the variability of AABW is essential for projecting changes in ocean circulation and for providing the basis for assessing potential risks

to global climate.

Appendix A. Neutral Density

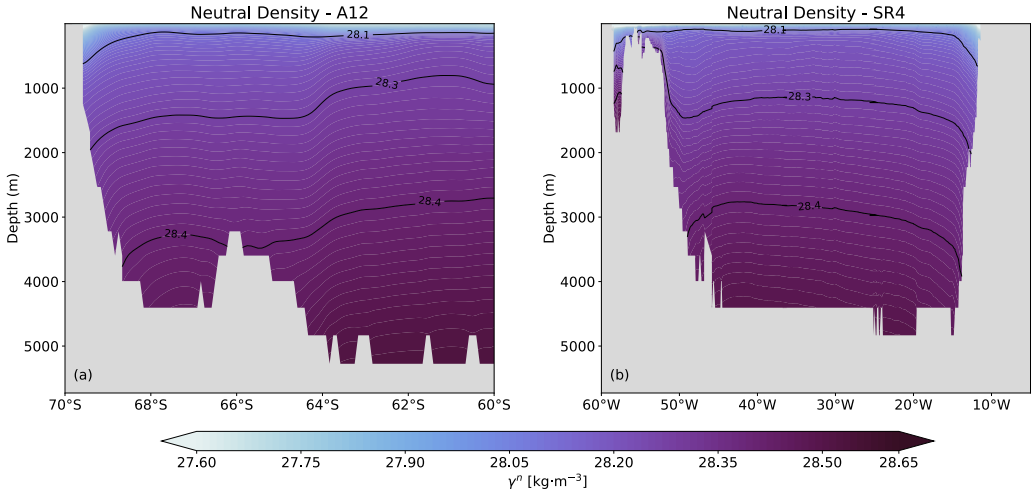

Figure A.1: **Mean neutral density structure along Sections A12 and SR4 (1993–2020).** (a) Neutral density cross-Section for Section A12 and (b) for Section SR4. Black contour lines indicate isopycnals at $\gamma^n = 28.10$ kg·m^{-3}, $\gamma^n = 28.27$ kg·m^{-3}, and $\gamma^n = 28.40$ kg·m^{-3}, corresponding to the layer boundaries of WDW ($\gamma^n = 28.10$ to 28.27 kg·m^{-3}), WSDW ($\gamma^n = 28.27$ to 28.40 kg·m^{-3}), and WSBW ($\gamma^n \geq 28.40$ kg·m^{-3}).

Appendix B. Complex MCA

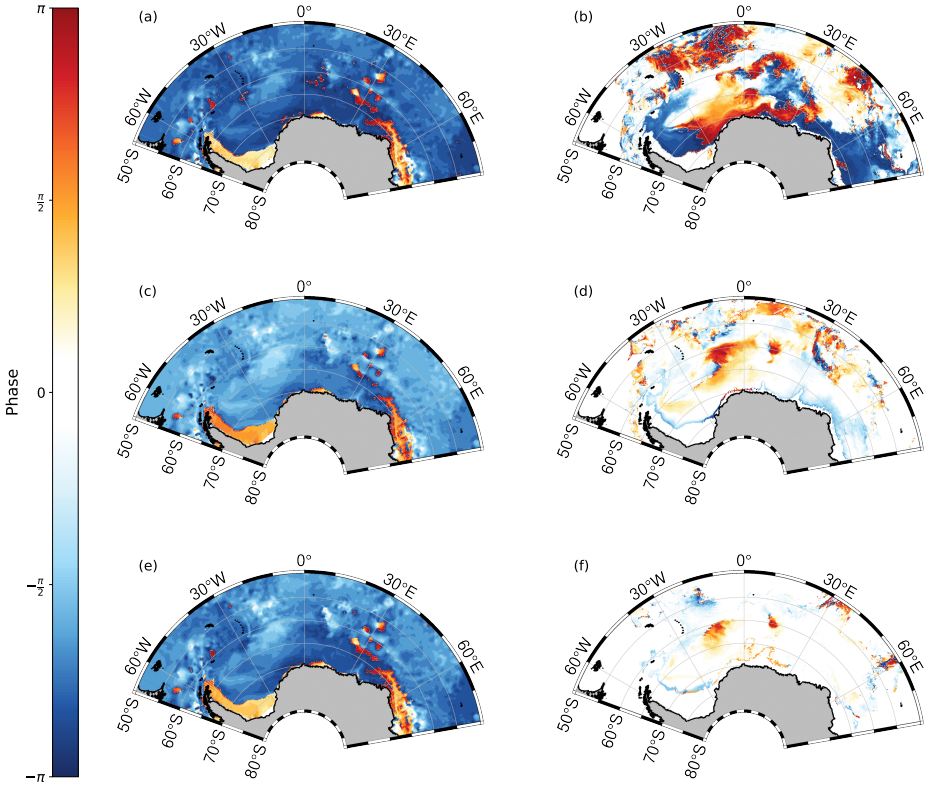

Figure B.1: **Phase analysis of the leading mode of covariability between the barotropic streamfunction (BSF) and potential temperature (θ).** Spatial phases of mode 1 of covariance between BSF (a, c, e) and θ of the (b) WDW, (d) WSDW, and (f) WSBW layers. Colors represent the phase (in radians) of the complex covariance patterns, showing the relative timing between BSF and temperature variability at each location. Regions with similar colors or values close to zero are approximately in phase, indicating synchronous variability, while opposite colors indicate that one variable leads or lags the other (yellow to red: one leads; light to dark blue: lag).

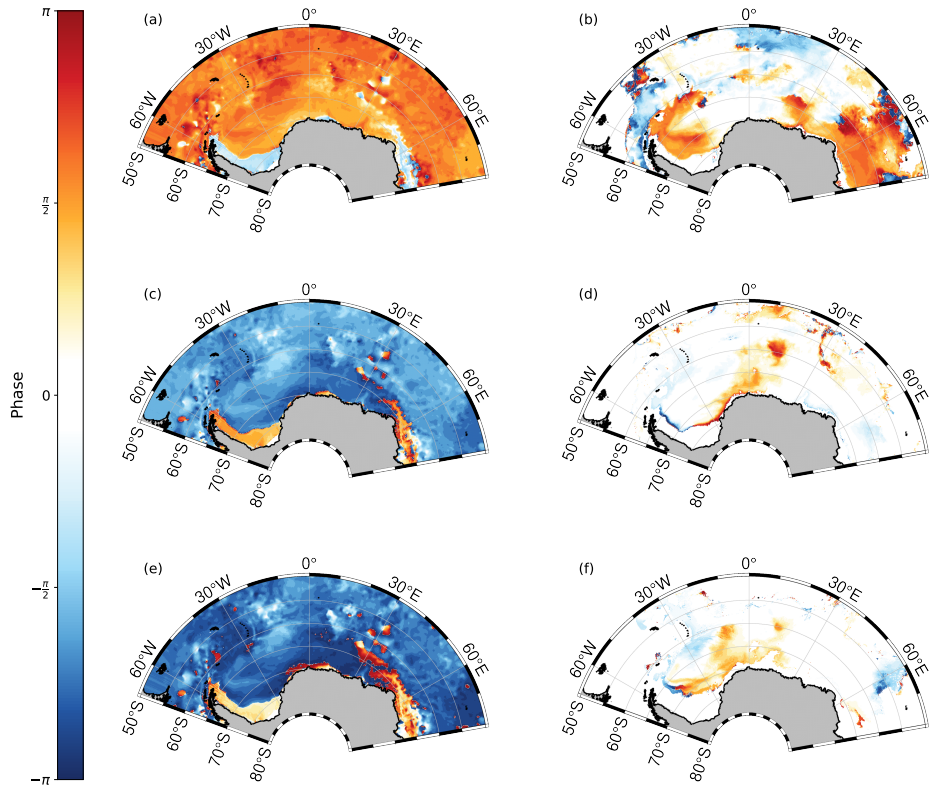

Figure B.2: **Phase analysis of the leading mode of covariability between the barotropic streamfunction (BSF) and salinity.** Spatial phases of mode 1 of covariance between BSF (a, c, e) and salinity of the (b) WDW, (d) WSDW, and (f) WSBW layers. Colors represent the phase (in radians) of the complex covariance patterns, showing the relative timing between BSF and temperature variability at each location. Regions with similar colors or values close to zero are approximately in phase, indicating synchronous variability, while opposite colors indicate that one variable leads or lags the other (yellow to red: one leads; light to dark blue: lag).

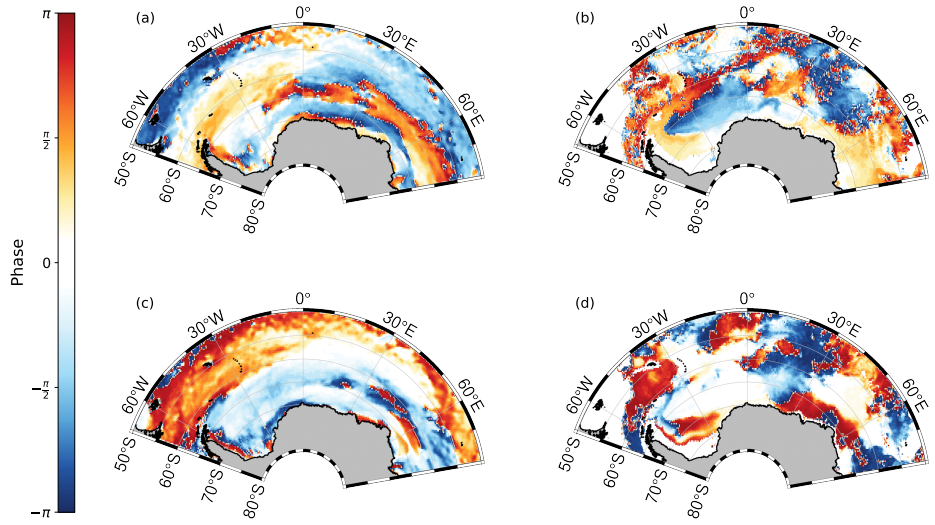

Figure B.3: **Phase analysis of the second mode of covariability between wind stress curl and WDW hydrographic properties.** Spatial phases of mode 2 of covariance between wind stress curl (a, c) and WDW (b) potential temperature (θ), and (d) salinity. Colors represent the phase (in radians) of the complex covariance patterns, showing the relative timing between wind stress curl and WDW properties at each location. Regions with similar colors or values close to zero are approximately in phase, indicating synchronous variability, while opposite colors indicate that one variable leads or lags the other (yellow to red: one leads; light to dark blue: lag).

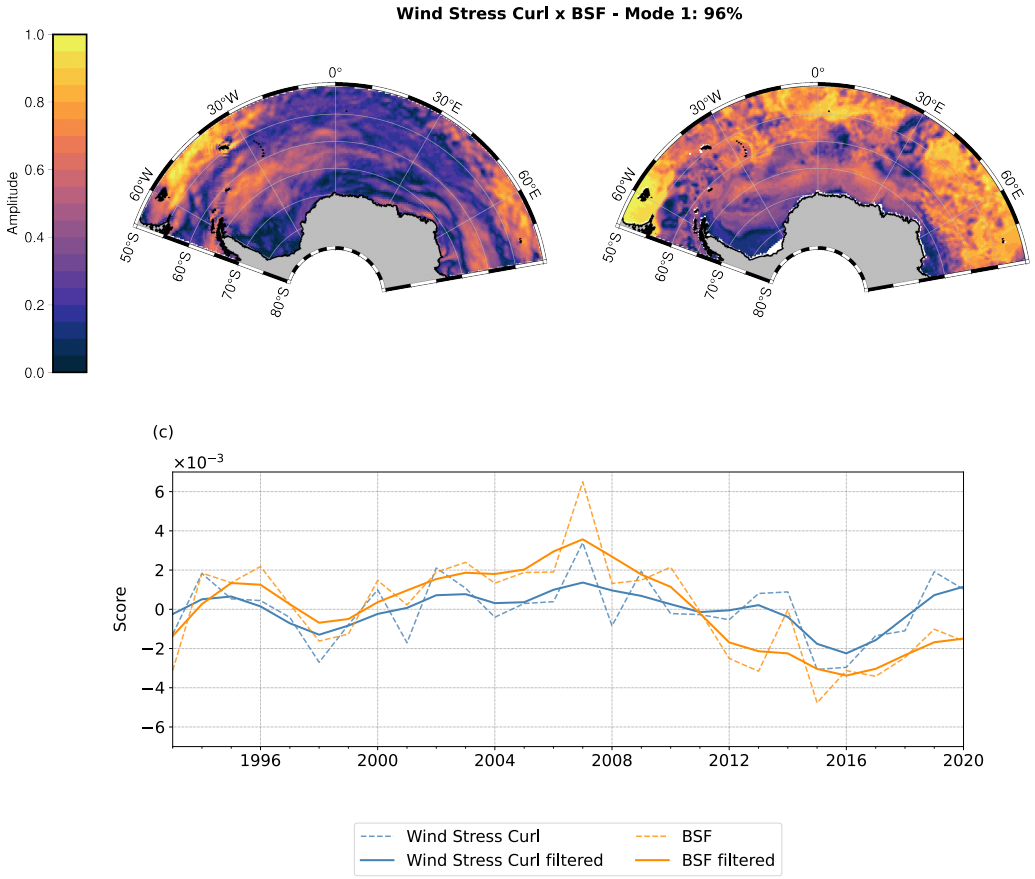

Figure B.4: **Leading mode of covariability between the wind stress curl and barotropic streamfunction (BSF).** Amplitudes of covariance associated with mode 1 between (a) the wind stress curl and (b) BSF. (c) Scores are plotted, showing only the real part, illustrating the temporal variation associated with mode 1 between the wind stress curl and BSF. In the spatial patterns, more yellowish tones indicate larger amplitudes of covariability.

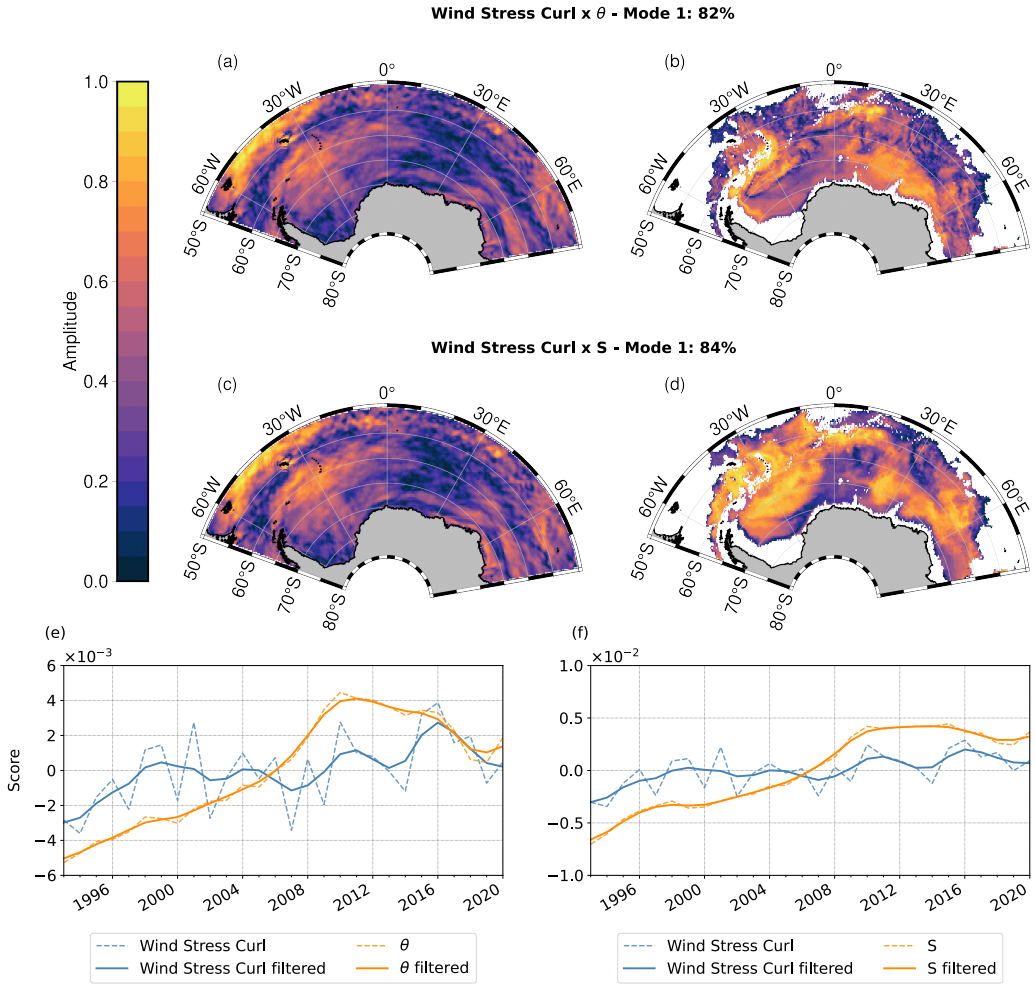

Figure B.5: **Leading mode of covariability between the wind stress curl and WSDW hydrographic properties.** Amplitudes of covariance associated with mode 1 between the wind stress curl (a, c) and WSDW potential temperature (θ) (b), and salinity (d). The corresponding scores are plotted, showing only the real part, illustrating the temporal variation associated with mode 1 between the wind stress curl and WSDW θ (e) and salinity (f). In the spatial patterns, more yellowish tones indicate larger amplitudes of covariability.

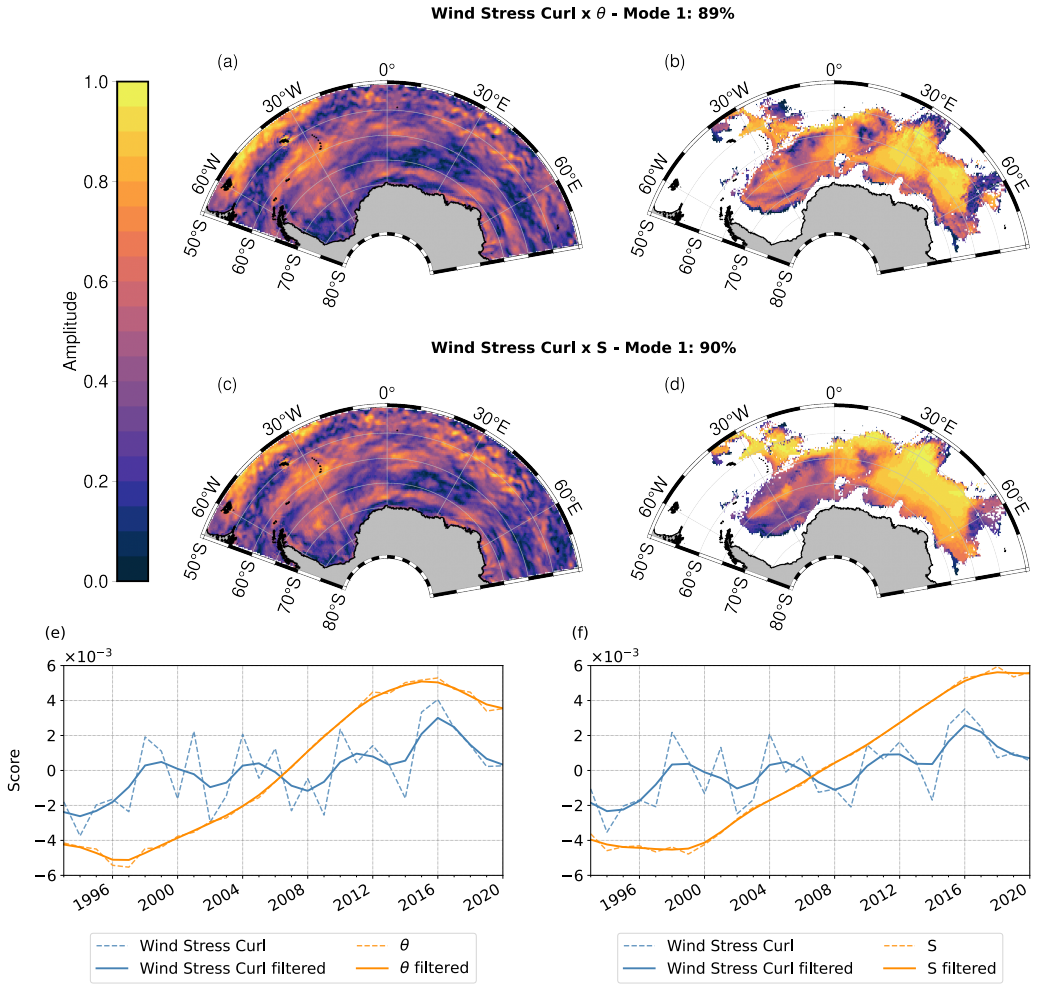

Figure B.6: **Leading mode of covariability between the wind stress curl and WSBW hydrographic properties.** Amplitudes of covariance associated with mode 1 between the wind stress curl (a, c) and WSBW potential temperature (θ) (b), and salinity (d). The corresponding scores are plotted, showing only the real part, illustrating the temporal variation associated with mode 1 between the wind stress curl and WSBW θ (e) and salinity (f). In the spatial patterns, more yellowish tones indicate larger amplitudes of covariability.

Appendix C. Weddell Gyre Barotropic Stream Function

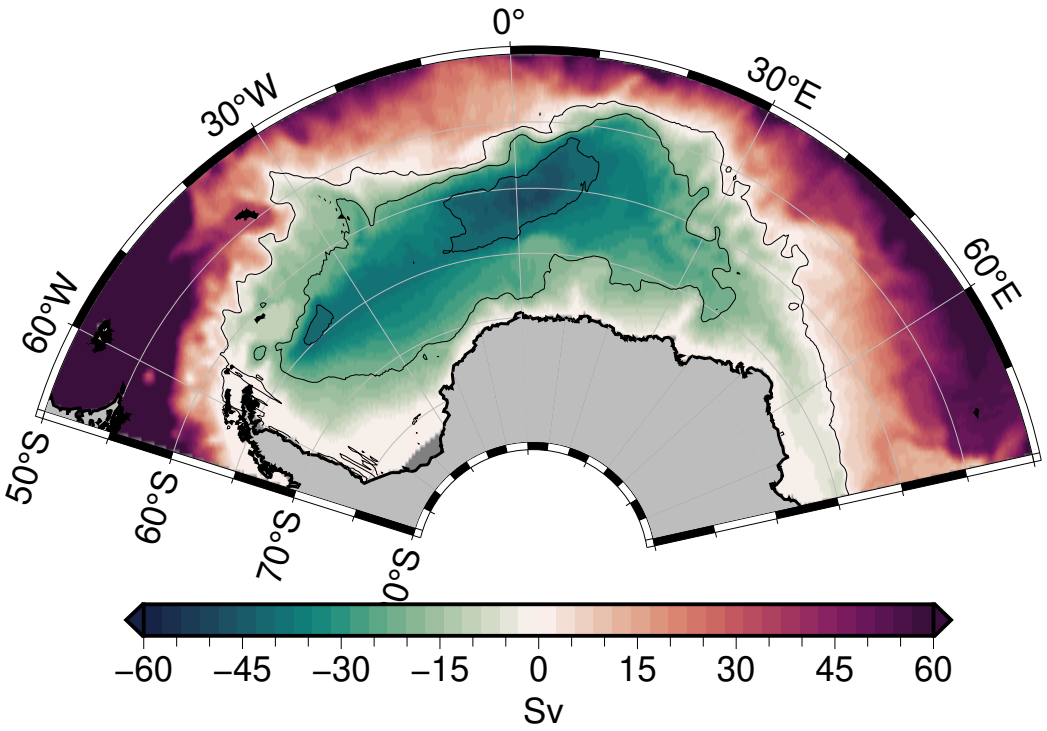

Figure C.1: **Mean state of barotropic streamfunction (BSF) in the Weddell Sea (1993–2020).**The BSF is calculated from the GLORYS2V4 product at 1/4° horizontal resolution (0.25° × 0.25°).

Appendix D. GLORYS12v1 Sea Ice Concentration

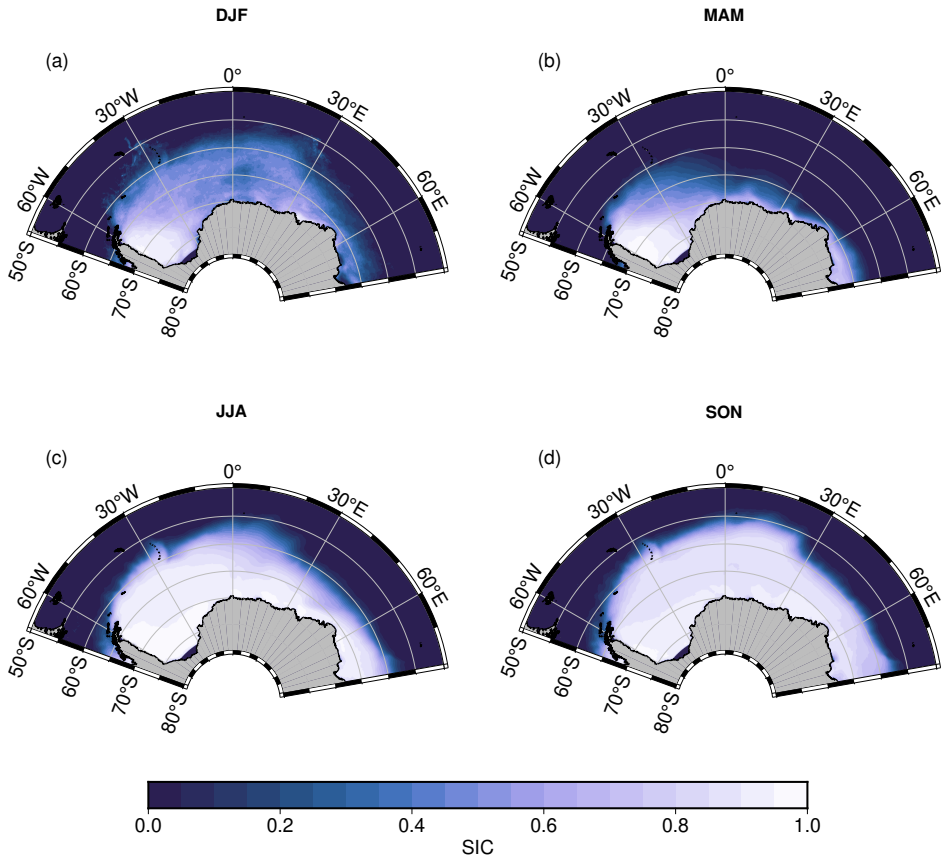

Figure D.1: **Seasonal mean sea ice concentration (SIC) from GLORYS12v1 (1993–2020).** The upper panels show SIC for (left) December–January–February (DJF) and (right) March–April–May (MAM), while the lower panels display SIC for (left) June–July–August (JJA) and (right) September–October–November (SON).

Acknowledgments

This study was supported in part by grants from Conselho Nacional de Desenvolvimento Científico e Tecnológico (CNPq) Process No: 141102/2022-5 and CNPq.MCT.INCT.CRIOSFERA-408461/2024-1. For the purpose of open access, the author(s) have applied a Creative Commons attribution (CC BY) license to any Author Accepted Manuscript version arising. TSD was supported by NERC National Capability programme AtlantiS (NE/Y005589/1). We acknowledge the Copernicus Marine Environment Monitoring Service (CMEMS) for developing and providing access to the GLORYS12v1 reanalysis data. We also acknowledge the efforts of the scientists, technicians, and data centers involved in creating and distributing the WOA18, especially the NOAA National Centers for Environmental Information (NCEI), as well as all the researchers who made their observational cruise data publicly available through the PANGAEA database.

Data Statement

Data access and information about GLORYS12v1 are available at `https://resources.marine.copernicus.eu/product-detail/GLOBAL_MULTIYEAR_PHY_001_030/INFORMATION`. The WOA18 climatology can be accessed at `https://www.ncei.noaa.gov/access/metadata/landing-page/bin/iso?id=gov.noaa.nodc:NCEI-WOA18`, and hydrographic data from the WOCE cruises are available via the PANGAEA database (`https://www.pangaea.de/`). For the complex MCA calculation, we used the open-source Python package xeofs (`https://xeofs.readthedocs.io`; Rieger and Levang, 2024; Rieger et al., 2024), and the PreTEOS-10 MATLAB toolbox (`https://www.teos-10.org/preteos10_software/neutral_density.html`) based on Jackett and McDougall (1997) algorithms to compute neutral density.

References

Abernathey, R.P., Cerovecki, I., Holland, P.R., Newsom, E., Mazloff, M., Talley, L.D., 2016. Water-mass transformation by sea ice in the upper branch of the Southern Ocean overturning. Nature Geoscience 9, 596–601. doi:10.1038/ngeo2749.

Aguiar, W., Mata, M.M., Kerr, R., 2017. On deep convection events and Antarctic Bottom Water formation in ocean reanalysis products. Ocean Science 13, 851–872. doi:10.5194/os-13-851-2017.

819 Amante, C., Eakins, B.W., 2009. ETOPO1 arc–minute global relief model:
820 procedures, data sources and analysis. Technical Memorandum NESDIS
821 NGDC-24. NOAA, National Geophysical Division Data Center, Marine
822 Geology and Geophysics. Boulder, Colorado. URL: https://repository.
823 library.noaa.gov/view/noaa/1163.

824 Armitage, T.W.K., Kwok, R., Thompson, A.F., Cunningham, G., 2018. Dy-
825 namic Topography and Sea Level Anomalies of the Southern Ocean: Vari-
826 ability and Teleconnections. Journal of Geophysical Research: Oceans 123,
827 613–630. doi:10.1002/2017JC013534.

828 Azaneu, M., Kerr, R., Mata, M.M., 2014. Assessment of the representation
829 of Antarctic Bottom Water properties in the ECCO2 reanalysis. Ocean
830 Science 10, 923–946. doi:10.5194/os-10-923-2014.

831 Azaneu, M., Kerr, R., Mata, M.M., Garcia, C.A.E., 2013. Trends in the deep
832 Southern Ocean (1958-2010): Implications for Antarctic Bottom Water
833 properties and volume export. Journal of Geophysical Research: Oceans
834 118, 4213–4227. doi:10.1002/jgrc.20303.

835 Becker, J., Sandwell, D., Smith, W., Braud, J., Binder, B., Depner, J.,
836 Fabre, D., Factor, J., Ingalls, S., Kim, S.H., Ladner, R., Marks, K.,
837 Nelson, S., Pharaoh, A., Trimmer, R., Von Rosenberg, J., Wallace,
838 G., Weatherall, P., 2009. Global bathymetry and elevation data at 30
839 arc seconds resolution: SRTM30_PLUS. Marine Geodesy 32, 355–371.
840 doi:10.1080/01490410903297766.

841 Behrens, E., Rickard, G., Morgenstern, O., Martin, T., Osprey, A., Joshi,
842 M., 2016. Southern Ocean deep convection in global climate models: A
843 driver for variability of subpolar gyres and Drake Passage transport on
844 decadal timescales. Journal of Geophysical Research: Oceans 121, 3905–
845 3925. doi:10.1002/2015JC011286.

846 Biló, T.C., Perez, R.C., Dong, S., Johns, W., Kanzow, T., 2024. Weak-
847 ening of the Atlantic Meridional Overturning Circulation abyssal limb
848 in the North Atlantic. Nature geoscience 17, 419–425. doi:10.1038/
849 s41561-024-01422-4.

850 Boyer, T., Baranova, O., Coleman, C., Garcia, H., Grodsky, A., Locarnini,
851 R., Mishonov, A., Paver, C., Reagan, J., Seidov, D., Smolyar, I., Weathers,

852 K., Zweng, M., 2018. World Ocean Database 2018. NOAA Atlas NESDIS
853 87 , 207 pp.A. V. Mishonov, Technical Editor.

854 Carmack, E.C., 1990. Large-Sacale Oceanography of Polar Oceans, in:
855 Smith, W.O.S. (Ed.), Polar Oceanography. Part A: Physical Science. Aca-
856 demic Press. chapter 4, pp. 171 – 211. doi:0.1016/B978-0-12-653031-5.
857 50009-6.

858 Carmack, E.C., Foster, T.D., 1975. On the flow of water out of the Wed-
859 dell Sea. Deep-Sea Research 22, 711–724. doi:10.1016/0011-7471(75)
860 90077-7.

861 Cerovečki, I., Talley, L.D., Mazloff, M.R., Maze, G., 2013. Subantarctic
862 Mode Water Formation, Destruction, and Export in the Eddy-Permitting
863 Southern Ocean State Estimate. Journal of Physical Oceanography 43,
864 1485 – 1511. doi:10.1175/JPO-D-12-0121.1.

865 Chen, J., Wilson, C., Tapley, B., Famiglietti, J., Rodell, M., 2005. Sea-
866 sonal global mean sea level change from satellite altimeter, GRACE,
867 and geophysical models. Journal of Geodesy 79, 532–539. doi:10.1007/
868 s00190-005-0005-9.

869 Daae, K., Hattermann, T., Darelius, E., Fer, I., 2017. On the effect of
870 topography and wind on warm water inflow-An idealized study of the
871 southern Weddell Sea continental shelf system. Journal of Geophysical
872 Research: Oceans 122, 2622–2641. doi:10.1002/2016JC012541.

873 Daae, K.L., Fer, I., Abrahamsen, E.P., 2009. Mixing on the continental slope
874 of the southern Weddell Sea. Journal of Geophysical Research: Oceans
875 114, C09018. doi:10.1029/2008JC005259.

876 Danabasoglu, G., Lamarque, J.F., Bacmeister, J., Bailey, D.A., DuVivier,
877 A.K., Edwards, J., Emmons, L.K., Fasullo, J., Garcia, R., Gettelman,
878 A., Hannay, C., Holland, M.M., Large, W.G., Lauritzen, P.H., Lawrence,
879 D.M., Lenaerts, J.T.M., Lindsay, K., Lipscomb, W.H., Mills, M.J., Neale,
880 R., Oleson, K.W., Otto-Bliesner, B., Phillips, A.S., Sacks, W., Tilmes, S.,
881 van Kampenhout, L., Vertenstein, M., Bertini, A., Dennis, J., Deser, C.,
882 Fischer, C., Fox-Kemper, B., Kay, J.E., Kinnison, D., Kushner, P.J., Lar-
883 son, V.E., Long, M.C., Mickelson, S., Moore, J.K., Nienhouse, E., Polvani,
884 L., Rasch, P.J., Strand, W.G., 2020. The community earth system model

version 2 (cesm2). Journal of Advances in Modeling Earth Systems 12, e2019MS001916. doi:https://doi.org/10.1029/2019MS001916.

Dotto, T.S., Kerr, R., Mata, M.M., Azaneu, M., Wainer, I., Fahrbach, E., Rohardt, G., 2014. Assessment of the structure and variability of Weddell Sea water masses in distinct ocean reanalysis prroducts. Ocean Science 10, 523–546. doi:10.5194/os-10-523-2014.

Dotto, T.S., Naveira Garabato, A., Bacon, S., Tsamados, M., Holland, P.R., Hooley, J., Frajka-Williams, E., Ridout, A., Meredith, M.P., 2018. Variability of the Ross Gyre, Southern Ocean: Drivers and responses revealed by satellite altimetry. Geophysical Research Letters 45, 6195–6204. doi:10.1029/2018GL078607.

Driemel, A., Fahrbach, E., Rohardt, G., Beszczynska-Möller, A., Boetius, A., Budéus, G., Cisewski, B., Engbrodt, R., Gauger, S., Geibert, W., Geprägs, P., Gerdes, D., Gersonde, R., Gordon, A.L., Grobe, H., Hellmer, H.H., Isla, E., Jacobs, S.S., Janout, M., Jokat, W., Klages, M., Kuhn, G., Meincke, J., Ober, S., Østerhus, S., Peterson, R.G., Rabe, B., Rudels, B., Schauer, U., Schröder, M., Schumacher, S., Sieger, R., Sildam, J., Soltwedel, T., Stangeew, E., Stein, M., Strass, V.H., Thiede, J., Tippenhauer, S., Veth, C., von Appen, W.J., Weirig, M.F., Wisotzki, A., Wolf-Gladrow, D.A., Kanzow, T., 2017. From pole to pole: 33 years of physical oceanography onboard r/v *Polarstern*. Earth System Science Data 9, 211–220. doi:10.5194/essd-9-211-2017.

Drévillon, M., Fernandez, E., Lellouche, J., 2022a. Product User Manual for the Global Ocean Physical Multi Year product GLOBAL_MULTIYEAR_PHY_001_030. doi:10.48670/moi-00021.

Drévillon, M., Lellouche, J., Régner, C., Garric, G., Bricaud, C., Hernandez, O., Bourdallé-Badie, R., 2022b. Quality Information Document for the Global Ocean Reanalysis Products GLOBAL_MULTIYEAR_PHY_001_030. doi:10.48670/moi-00021.

Ezer, T., Mellor, G.L., 2004. A generalized coordinate ocean model and a comparison of the bottom boundary layer dynamics in terrain-following and in z-level grids. Ocean Modelling 6, 379–403. doi:10.1016/S1463-5003(03)00026-X.

Fahrbach, E., Hoppema, M., Rohardt, G., Boebel, O., Klatt, O., Wisotzki, A., 2011. Warming of deep and abyssal water masses along the Greenwich meridian on decadal time scales: The Weddell gyre as a heat buffer. Deep Sea Research Part II: Topical Studies in Oceanography 58, 2509–2523. doi:10.1016/j.dsr2.2011.06.007.

Fahrbach, E., Hoppema, M., Rohardt, G., Schröder, M., Wisotzki, A., 2004. Decadal-scale variations of water mass properties in the deep Weddell Sea. Ocean Dynamics 54, 77–91. doi:10.1007/s10236-003-0082-3.

Fahrbach, E., Petterson, R.G., Rohardt, G., Scholosser, P., Bayers, R., 1994. Suppression of bottom water formation in the southeastern Weddell Sea. Deep-Sea Research Part I: Oceanographic Research Papers 41, 389–411. doi:10.1016/0967-0637(94)90010-8.

Fahrbach, E., Rohardt, G., 1993. Physical oceanography during POLARSTERN cruise ANT-X/7 on section SR04, PANGAEA. doi:10.1594/PANGAEA.742651. in supplement to: Hellmer, Hartmut H; Huhn, Oliver; Gomis, Damià; Timmermann, Ralph (2011): On the freshening of the northwestern Weddell Sea continental shelf. Ocean Science, 7(3), 305-316, https://doi.org/10.5194/os-7-305-2011.

Fahrbach, E., Rohardt, G., 1996. Physical oceanography during POLARSTERN cruise ANT-XIII/4 on section S04A, PANGAEA. doi:10.1594/PANGAEA.738489. in supplement to: Hellmer, Hartmut H; Huhn, Oliver; Gomis, Damià; Timmermann, Ralph (2011): On the freshening of the northwestern Weddell Sea continental shelf. Ocean Science, 7(3), 305-316, https://doi.org/10.5194/os-7-305-2011.

Fahrbach, E., Rohardt, G., 1998. Physical oceanography during POLARSTERN cruise ANT-XV/4 (DOVETAIL) on section SR04, PANGAEA. doi:10.1594/PANGAEA.742626. in supplement to: Hellmer, Hartmut H; Huhn, Oliver; Gomis, Damià; Timmermann, Ralph (2011): On the freshening of the northwestern Weddell Sea continental shelf. Ocean Science, 7(3), 305-316, https://doi.org/10.5194/os-7-305-2011.

Fahrbach, E., Rohardt, G., 2008. Physical oceanography during POLARSTERN cruise ANT-XXIV/3, PANGAEA. doi:10.1594/PANGAEA.733414. in supplement to: Hellmer, Hartmut H; Huhn, Oliver; Gomis,

951 Damià; Timmermann, Ralph (2011): On the freshening of the north-
952 western Weddell Sea continental shelf. Ocean Science, 7(3), 305-316,
953 https://doi.org/10.5194/os-7-305-2011.

954 Fichefet, T., Maqueda, M.A.M., 1997. Sensitivity of a global sea ice model
955 to the treatment of ice thermodynamics and dynamics. Journal of Geo-
956 physical Research: Oceans 102, 12609–12646. doi:10.1029/97JC00480.

957 Flexas, M.d.M., Schodlok, M.P., Padman, L., Menemenlis, D., Orsi, A.H.,
958 2015. Role of tides on the formation of the A ntarctic Slope Front at the
959 Weddell-Scotia Confluence. Journal of Geophysical Research: Oceans 120,
960 3658–3680. doi:10.1002/2014JC010372.

961 Garcia, H., Boyer, T., Baranova, O., Locarnini, R., Mishonov, A., Grodsky,
962 A., Paver, C., Weathers, K., Smolyar, I., Reagan, J., Seidov, D., Zweng,
963 M., 2019. World Ocean Atlas 2018: Product Documentation. A. Mishonov,
964 Technical Editor.

965 Good, S.A., Martin, M.J., Rayner, N.A., 2013. EN4: Quality controlled
966 ocean temperature and salinity profiles and monthly objective analyses
967 with uncertainty estimates. Journal of Geophysical Research: Oceans 118,
968 6704–6716. doi:10.1002/2013JC009067.

969 Goosse, H., Fichefet, T., 1999. Importance of ice-ocean interactions for the
970 global ocean circulation: A model study. Journal of Geophysical Research:
971 Oceans 104, 23337–23355. doi:10.1029/1999JC900215.

972 Hattermann, T., Smedsrud, L.H., Nøst, O.A., Lilly, J.M., Galton-Fenzi, B.K.,
973 2014. Eddy-resolving simulations of the Fimbul Ice Shelf cavity circulation:
974 Basal melting and exchange with open ocean. Ocean Modelling 82, 28–44.
975 doi:10.1016/j.ocemod.2014.07.004.

976 Hersbach, H., Bell, B., Berrisford, P., Hirahara, S., Horányi, A., Muñoz-
977 Sabater, J., Nicolas, J., Peubey, C., Radu, R., Schepers, D., et al., 2020.
978 The ERA5 global reanalysis. Quarterly Journal of the Royal Meteorological
979 Society 146, 1999–2049. doi:10.1002/qj.3803.

980 Heuzé, C., 2021. Antarctic Bottom Water and North Atlantic Deep Water in
981 CMIP6 models. Ocean Science 17, 59–90. doi:10.5194/os-17-59-2021.

Hogg, A.M.C., Meredith, M.P., Chambers, D.P., Abrahamsen, E.P., Hughes, C.W., Morrison, A.K., 2015. Recent trends in the Southern Ocean eddy field. Journal of Geophysical Research: Oceans 120, 257–267. doi:10.1002/2014JC010470.

Huang, B., Liu, C., Banzon, V., Freeman, E., Graham, G., Hankins, B., Smith, T., Zhang, H.M., 2021. Improvements of the Daily Optimum Interpolation Sea Surface Temperature (DOISST) Version 2.1. Journal of Climate 34, 2923 – 2939. doi:10.1175/JCLI-D-20-0166.1.

Jackett, D.R., McDougall, T.J., 1997. A neutral density variable for the world's oceans. Journal of Physical Oceanography 27, 237–263. doi:10.1175/1520-0485(1997)027\%3C0237:ANDVFT\%3E2.0.CO;2.

Jayne, S.R., Roemmich, D., Zilberman, N., Riser, S.C., Johnson, K.S., Johnson, G.C., Piotrowicz, S.R., 2017. The Argo Program: Present and Future. Oceanography 30, 18–28. URL: http://www.jstor.org/stable/26201840.

Johnson, G.C., Lyman, J.M., Purkey, S.G., 2015. Informing Deep Argo array design using Argo and full-depth hydrographic section data. Journal of Atmospheric and Oceanic Technology 32, 2187–2198. doi:https://doi.org/10.1175/JTECH-D-15-0139.1.

Jullion, L., Naveira Garabato, A.C., Bacon, S., Meredith, M.P., Brown, P.J., Torres-Valdés, S., Speer, K.G., Holland, P.R., Dong, J., Bakker, D., Hoppema, M., Loose, B., Venables, H.J., Jenkins, W.J., Messias, M.J., Fahrbach, E., 2014. The contribution of the Weddell Gyre to the lower limb of the Global Overturning Circulation. Journal of Geophysical Research: Oceans 119, 3357–3377. doi:10.1002/2013JC009725.

Kerr, R., Dotto, T.S., Mata, M.M., Hellmer, H.H., 2018. Three decades of deep water mass investigation in the Weddell Sea (1984–2014): Temporal variability and changes. Deep Sea Research Part II: Topical Studies in Oceanography 149, 70–83. doi:10.1016/j.dsr2.2017.12.002.

Kerr, R., Mata, M.M., Garcia, C.A.E., 2009. On the temporal variability of the Weddell Sea Deep Water masses. Antarctic Science 21, 383–400. doi:10.1017/S0954102009001990.

Klatt, O., Fahrbach, E., Hoppema, M., Rohardt, G., 2005. The transport of the Weddell Gyre across the Prime Meridian. Deep Sea Research Part II: Topical Studies in Oceanography 52, 513–528. doi:10.1016/j.dsr2.2004.12.015.

Large, W.G., Yeager, S.G., 2009. The global climatology of an interannually varying air–sea flux data set. Climate Dynamics 33, 341–364. doi:10.1007/s00382-008-0441-3.

Le Paih, N., Hattermann, T., Boebel, O., Kanzow, T., Lüpkes, C., Rohardt, G., Strass, V., Herbette, S., 2020. Coherent Seasonal Acceleration of the Weddell Sea Boundary Current System Driven by Upstream Winds. Journal of Geophysical Research: Oceans 125, e2020JC016316. doi:10.1029/2020JC016316.

Lellouche, J., Le Galloudec, O., Régner, C., Van Gennip, S., Law Chune, S., Levier, B., Greiner, E., Drévillon, M., Szczypta, C., 2025. Quality Information Document for the Global Production Centre GLO_ANALYSISFORECAST_PHY_001_024. doi:10.48670/moi-00016.

Lellouche, J.M., Greiner, E., Bourdallé-Badie, R., Garric, G., Melet, A., Drevillon, M., Bricaud, C., Hamon, M., Le Galloudec, O., Regnier, C., Candela, T., Testut, C.E., Gasparin, F., Ruggiero, G., Benkiran, M., Drillet, Y., Le Traon, P.Y., 2021. The Copernicus Global 1/12° Oceanic and Sea Ice GLORYS12 Reanalysis. Frontiers in Earth Science 9, 698876. doi:10.3389/feart.2021.698876.

Lellouche, J.M., Greiner, E., Le Galloudec, O., Garric, G., Regnier, C., Drevillon, M., Benkiran, M., Testut, C.E., Bourdalle-Badie, R., Gasparin, F., Hernandez, O., Levier, B., Drillet, Y., Remy, E., Le Traon, P.Y., 2018. Recent updates to the Copernicus Marine Service global ocean monitoring and forecasting real-time 1/12° high-resolution system. Ocean Science 14, 1093–1126. doi:10.5194/os-14-1093-2018.

Li, Q., England, M.H., Hogg, A.M., Rintoul, S.R., Morrison, A.K., 2023. Abyssal ocean overturning slowdown and warming driven by Antarctic meltwater. Nature 615, 841–847. doi:10.1038/s41586-023-05762-w.

Locarnini, R., Mishonov, A., Antonov, J., Boyer, T., H.E., G., Baranova, O., Zweng, M., Paver, C., Reagan, J., Johnson, D., Hamilton, D., Seidov, D., 2013. World Ocean Atlas 2013, Volume 1: Temperature. NOAA Atlas NESDIS 73 , 40 pp.S. Levitus, Ed.; A. Mishonov, Technical Ed.

Locarnini, R., Mishonov, A., Baranova, O., Boyer, T., Zweng, M., Garcia, H., Reagan, J., Seidov, D., Weathers, K., Paver, C., Smolyar, I., 2019. World Ocean Atlas 2018, Volume 1: Temperature. NOAA Atlas NESDIS 81 , 52 pp.A. Mishonov, Technical Editor.

Lumpkin, R., Speer, K., 2007. Global Ocean Meridional Overturning. Journal of Physical Oceanography 37, 2550–2562. doi:10.1175/JPO3130.1.

Madec, G., Imbard, M., 1996. A global ocean mesh to overcome the North Pole singularity. Climate Dynamics 12, 381–388. doi:10.1007/BF00211684.

Madec, G., The NEMO Team, 2008. NEMO Ocean Engine. Note du Pôle de modélisation. France: Institut Pierre-Simon Laplace (IPSL), 1288–1619.

Mazloff, M.R., Heimbach, P., Wunsch, C., 2010. An Eddy-Permitting Southern Ocean State Estimate. Journal of Physical Oceanography 40, 880 – 899. doi:10.1175/2009JPO4236.1.

Meredith, M.P., Locarnini, R.A., Van Scoy, K.A., Watson, A.J., Heywood, K.J., King, B.A., 2000. On the sources of Weddell Gyre Antarctic Bottom Water. Journal of Geophysical Research 105, 1093–1104. doi:10.1029/1999JC900263.

Mohrmann, M., Heuzé, C., Swart, S., 2021. Southern Ocean polynyas in CMIP6 models. Cryosphere 15, 4281–4313. doi:10.5194/tc-15-4281-2021.

Morrison, A.K., Hogg, A.M., England, M.H., Spence, P., 2020. Warm Circumpolar Deep Water transport toward Antarctica driven by local dense water export in canyons. Science Advances 6, eaav2516. doi:10.1126/sciadv.aav2516.

Nakayama, Y., Malyarenko, A., Zhang, H., Wang, O., Auger, M., Nie, Y., Fenty, I., Mazloff, M., Köhl, A., Menemenlis, D., 2024. Evaluation of

MITgcm-based ocean reanalyses for the Southern Ocean. Geoscientific Model Development 17, 8613–8638. doi:10.5194/gmd-17-8613-2024.

Narayanan, A., Gille, S.T., Mazloff, M.R., du Plessis, M.D., Murali, K., Roquet, F., 2023. Zonal distribution of Circumpolar Deep Water transformation rates and its relation to heat content on Antarctic shelves. Journal of Geophysical Research: Oceans 128, e2022JC019310.

Naveira Garabato, A.C., Dotto, T.S., Hooley, J., Bacon, S., Tsamados, M., Ridout, A., Frajka-Williams, E.E., Herraiz-Borreguero, L., Holland, P.R., Heorton, H.D., Meredith, M.P., 2019. Phased Response of the Subpolar Southern Ocean to Changes in Circumpolar Winds. Geophysical Research Letters 46, 6024–6033. doi:10.1029/2019GL082850.

Naveira Garabato, A.C., McDonagh, E.L., Stevens, D.P., Heywood, K.J., Sanders, R.J., 2002. On the export of Antarctic bottom water from the Weddell Sea. Deep Sea Research Part II: Topical Studies in Oceanography 49, 4715–4742. doi:10.1016/S0967-0645(02)00156-X.

Naveira Garabato, A.C., Zika, J.D., Jullion, L., Brown, P.J., Holland, P.R., Meredith, M.P., Bacon, S., 2016. The thermodynamic balance of the Weddell Gyre. Geophysical Research Letters 43, 317–325. doi:10.1002/2015GL066658.

Neme, J., England, M.H., Hogg, A.M., 2021. Seasonal and Interannual Variability of the Weddell Gyre From a High-Resolution Global Ocean-Sea Ice Simulation During 1958–2018. Journal of Geophysical Research: Oceans 126, e2021JC017662. doi:10.1029/2021JC017662.

Nøst, O.A., Biuw, M., Tverberg, V., Lydersen, C., Hattermann, T., Zhou, Q., Smedsrud, L.H., Kovacs, K.M., 2011. Eddy overturning of the Antarctic Slope Front controls glacial melting in the Eastern Weddell Sea. Journal of Geophysical Research: Oceans 116. doi:10.1029/2011JC006965.

Oelerich, R., Heywood, K.J., Damerell, G.M., Thompson, A.F., 2022. Wind-Induced Variability of Warm Water on the Southern Bellingshausen Sea Continental Shelf. Journal of Geophysical Research: Oceans 127, e2022JC018636. doi:10.1029/2022JC018636.

Orsi, A.H., Nowlin, W.D., Whitworth, T., 1993. On the circulation and stratification of the Weddell Gyre. Deep Sea Research 40, 169–203. doi:0.1016/0967-0637(93)90060-G.

Pujol, M.I., Faugère, Y., Taburet, G., Dupuy, S., Pelloquin, C., Ablain, M., Picot, N., 2016. DUACS DT2014: the new multi-mission altimeter data set reprocessed over 20 years. Ocean Science 12, 1067–1090. doi:10.5194/os-12-1067-2016.

Purkey, S.G., Johnson, G.C., 2010. Warming of Global Abyssal and Deep Southern Ocean Waters between the 1990s and 2000s: Contributions to Global Heat and Sea Level Rise Budgets. Journal of Climate 23, 6336–6351. doi:10.1175/2010JCLI3682.1.

Purkey, S.G., Johnson, G.C., 2012. Global Contraction of Antarctic Bottom Water between the 1980s and 2000s. Journal of Climate 25, 5830–5844. doi:10.1175/JCLI-D-11-00612.1.

Reeve, K.A., Boebel, O., Strass, V., Kanzow, T., Gerdes, R., 2019. Horizontal circulation and volume transports in the Weddell Gyre derived from Argo float data. Progress in Oceanography 175, 263–283. doi:10.1016/j.pocean.2019.04.006.

Rieger, N., Álvaro Corral, Olmedo, E., Turiel, A., 2021. Lagged Teleconnections of Climate Variables Identified via Complex Rotated Maximum Covariance Analysis. Journal of Climate 34, 9861–9878. doi:10.1175/JCLI-D-21-0244.1.

Rieger, N., Levang, S.J., 2024. xeofs: Comprehensive EOF analysis in Python with xarray. Journal of Open Source Software 9. doi:10.21105/joss.06060.

Rieger, N., Levang, S.J., et al., 2024. xeofs: v2.3.2. doi:10.5281/zenodo.10897729.

Rohardt, G., 2010. Physical oceanography during POLARSTERN cruise ANT-XXII/3. doi:10.1594/PANGAEA.733664.

Rohardt, G., 2013. Physical oceanography during POLARSTERN cruise ANT-XXIX/2. doi:10.1594/PANGAEA.817255.

Rohardt, G., Boebel, O., 2015. Physical oceanography during POLARSTERN cruise PS89 (ANT-XXX/2). doi:10.1594/PANGAEA.846701.

Rohardt, G., Fahrbach, E., Wisotzki, A., 2011. Physical oceanography during POLARSTERN cruise ANT-XXVII/2. doi:10.1594/PANGAEA.772244.

Rohardt, G., Harms, S., 2010. Physical oceanography during POLARSTERN cruise ANT-XVI/2. doi:10.1594/PANGAEA.735530.

Ryan, S., Schröder, M., Huhn, O., Timmermann, R., 2016. On the warm inflow at the eastern boundary of the Weddell Gyre. Deep Sea Research Part I: Oceanographic Research Papers 107, 70–81. doi:10.1016/j.dsr.2015.11.002.

Schröder, M., 2010. Physical oceanography during POLARSTERN cruise ANT-XVIII/3. doi:10.1594/PANGAEA.742584.

Schröder, M., Wisotzki, A., 2010. Physical oceanography during POLARSTERN cruise ANT-XX/2. doi:10.1594/PANGAEA.738486.

Schröder, M., Fahrbach, E., 1999. On the structure and the transport of the eastern Weddell Gyre. Deep Sea Research Part II: Topical Studies in Oceanography 46, 501–527. doi:10.1016/S0967-0645(98)00112-X.

van Sebille, E., Spence, P., Mazloff, M.R., England, M.H., Rintoul, S.R., Saenko, O.A., 2013. Abyssal connections of Antarctic Bottom Water in a Southern Ocean State Estimate. Geophysical Research Letters 40, 2177–2182. doi:https://doi.org/10.1002/grl.50483.

Stewart, A.L., Klocker, A., Menemenlis, D., 2019. Acceleration and overturning of the antarctic slope current by winds, eddies, and tides. Journal of Physical Oceanography 49, 2043–2074. doi:10.1175/JPO-D-18-0221.1.

Strass, V.H., Rohardt, G., Kanzow, T., Hoppema, M., Boebel, O., 2020. Multidecadal warming and density loss in the Deep Weddell Sea, Antarctica. Journal of Climate 33, 9863–9881. doi:10.1175/JCLI-D-20-0271.1.

Szekely, T., Gourrion, J., Pouliquen, S., Reverdin, G., 2023. CORA, Coriolis Ocean Dataset for Reanalysis. SEANOE. doi:10.17882/46219.

1168 Talley, L.D., 2013. Closure of the global overturning circulation through
1169 the Indian, Pacific, and Southern Oceans: Schematics and transports.
1170 Oceanography 26, 80–97. doi:10.5670/oceanog.2013.07.

1171 Thompson, A.F., Heywood, K.J., Schmidtko, S., Stewart, A.L., 2014. Eddy
1172 transport as a key component of the Antarctic overturning circulation.
1173 Nature Geoscience 7, 171–180. doi:10.1038/NGEO2289.

1174 Tonelli, M., Marcello, F., Ferrero, B., Wainer, I., 2019. Warm Deep Water
1175 Variability During the Last Millennium in the CESM–LME: Pre-Industrial
1176 Scenario versus Late 20th Century Changes. Geosciences 9, 346. doi:10.
1177 3390/geosciences9080346.

1178 Tsamados, M., Feltham, D.L., Schroeder, D., Flocco, D., Farrell, S.L., Kurtz,
1179 N., Laxon, S.W., Bacon, S., 2014. Impact of Variable Atmospheric and
1180 Oceanic Form Drag on Simulations of Arctic Sea Ice. Journal of Physical
1181 Oceanography 44, 1329 – 1353. doi:10.1175/JPO-D-13-0215.1.

1182 Verdy, A. and Mazloff, M. R., 2017. A data assimilating model for estimat-
1183 ing Southern Ocean biogeochemistry. Journal of Geophysical Research:
1184 Oceans 122, 6968–6988. doi:https://doi.org/10.1002/2016JC012650.

1185 Vernet, M., Geibert, W., Hoppema, M., Brown, P.J., Haas, C., Hellmer,
1186 H.H., Jokat, W., Jullion, L., Mazloff, M., Bakker, D.C.E., Brearley,
1187 J.A., Croot, P., Hattermann, T., Hauck, J., Hillenbrand, C.D., Hoppe,
1188 C.J.M., Huhn, O., Koch, B.P., Lechtenfeld, O.J., Meredith, M.P., Naveira
1189 Garabato, A.C., Nöthig, E.M., Peeken, I., Rutgers van der Loeff, M.M.,
1190 Schmidtko, S., Schröder, M., Strass, V.H., Torres-Valdés, S., Verdy, A.,
1191 2019. The Weddell Gyre, Southern Ocean: Present Knowledge and
1192 Future Challenges. Reviews of Geophysics 57, 623–708. doi:10.1029/
1193 2018RG000604.

1194 Wainer, I., Gent, P.R., 2019. Changes in the Atlantic Sector of the Southern
1195 Ocean estimated from the CESM Last Millennium Ensemble. Antarctic
1196 Science 31, 37–51. doi:10.1017/S0954102018000433.

1197 Whitworth, T., Orsi, A.H., Kim, S.J., Nowlin, W.D., Locarnini, R.A., 1998.
1198 Water Masses and Mixing Near the Antarctic Slope Front, in: Jacobs,
1199 S.S., Weiss, R.F. (Eds.), Ocean, Ice, and Atmosphere: Interactions at the

Antarctic Continental Margin. American Geophysical Union. volume 75, pp. 1–27. doi:10.1029/AR075p0001.

Zhou, S., Meijers, A.J.S., Meredith, M.P., Abrahamsen, E.P., Holland, P.R., Silvano, A., Sallée, J.B., Østerhus, S., 2023. Slowdown of Antarctic Bottom Water export driven by climatic wind and sea-ice changes. Nature Climate Change 13, 701–709. doi:10.1038/s41558-023-01695-4.

Zweng, M., Reagan, J., Seidov, D., Boyer, T., Locarnini, R., , Garcia, H., Mishonov, A., Baranova, O., Weathers, K., Paver, C., Smolyar, I., 2019. World Ocean Atlas 2018, Volume 2: Salinity. NOAA Atlas NESDIS 82 , 50 pp.A. Mishonov, Technical Editor.